Estimation of Polar Depletion Regions by VTEC Contrast and Watershed Enhancing

Enrique Monte-Moreno[1], Manuel Hernandez-Pajares[2], Haixia Lyu[2], Heng Yang[3], and Angela Aragon-Angel[4,]

***Abstract*—This article presents a method for determining near-pole ionization depletion regions and troughs from GNSS VTEC maps. To define the regions, we use Image processing tools, considering the VTEC maps as grey level images. In this work, watershed segmentation is applied to determine the edges of regions, based on the flow of areas between the lowest ionization zones ($< 1\%$) and the medium ionization regions ($> 10\%$). In order to enhance the contrast between low-ionization regions and those with a higher relative ionization, the histogram of the maps is equalized, which increases the contrast of the VTEC maps, which is the distance between low-ionization regions and those with a higher relative ionization is increased. The use of percentile thresholds makes this method independent of hypotheses about the generation of depletions, their morphology, or about the number of depletion regions that can occur on a map. We test the performance by comparing the depletion regions identified in eight events reported in the literature under different conditions of the ionosphere. The events used as reference were measured by satellites, radar, and GNSS. The method we propose allows for real-time processing of GNSS VTEC maps. The morphology of the detected regions matches the shape that is reported in the literature.**

***Index Terms*—Polar depletion; Polar Trough; Image segmentation; Watershed algorithm; Histogram equalization.**

I. Introduction

We present a method for determining depletion regions at the polar ionosphere. Unlike other works dealing with ionospheric depletions (for instance [Rodger (1992)], [Moffett (1983)], [voiculescu (2016)]) we will not postulate hypotheses about the origins or describe the physics of the phenomena, and will restrict ourselves to proposing a way of determining the morphology associated with depletion regions. Another feature of this article is that we will rely only on Global Ionospheric Maps (GIM) of Vertical Total Electron Content (VTEC) computed from GNSS measurements, while the publications we have used as benchmarks to confirm the performance of our method, make use of higher resolution information from specific satellites, radar and also GNSS.

The definition of *depletion region* that we will use in this article will be similar to that of the troughs in the ionosphere. We will restrict ourselves to defining depletion as a relative decrease in the level of ionization, without relating it to specific events such as storms, etc. In [Rodger (1992)], [voiculescu (2016)] for instance, troughs are defined as regions where the plasma concentration is lower compared to the immediately neighboring regions towards the pole or the equator. It is also defined as a few degrees of latitude in terms of width. We will limit the definition of the depletion region to a relative decrease in the VTEC level covering the lower percentile of the VTEC range. We will not place restrictions on the morphology, allowing even the presence of disconnected depletion regions.

The method for identifying the depletion regions relies on an image processing tool that uses a fluid mechanics metaphor. In this metaphor, the regions are determined by the points of intermediate ionization that flow in a direction competing with points of *very low* ionization that flow on the contrary direction generating a stability region that will cover areas of low ionization, with a flexible morphology. This flexibility in determining morphology explains the shape of the depletion as elongated regions in different directions or independent regions of depletion separated by regions with higher ionization.

Thus, in this article, we will extend the definition of a trough to that of depletion, and we will define the region of depletion as a region in which there is a decrease in plasma and with arbitrary morphology and without offering physical explanations. We will use as a proxy to the plasma level the VTEC calculated via GNSS, and interpolated between the pierce points.

Since we will not make hypotheses about the origins of depletion. The depletion is a phenomenon that is relative to surrounding regions that depend on various factors, such as the season, the solar cycle, geomagnetic conditions, etc. we will define the depletion thresholds based on VTEC percentiles. An additional reason that justifies the use of percentiles is the fact that taking the 1% VTEC percentile as a reference point, our algorithm provides depletion regions that cover between 2% and 10% of the pole area under study. The average value of VTEC in the areas covered by the depletion was 2-3 times lower than the mean value outside the depletion, as summarized in section VIII-A for the cases studied in this paper.

The fact that the depletion is defined as a relative change is clear from the figures that indicate the temporal evolution of the minimum VTEC, average VTEC in the region detected as depletion, and the average value outside the depletion region (see examples in Section VIII). In the examples where a trough is measured and a storm occurs at the same time, when a trough is reported in the literature the three VTEC values mentioned above hardly change, however, the area of the

[1]Department of Signal Theory and Communications, TALP, Universitat Politècnica de Catalunya, 08034 Barcelona, Spain; enric.monte@upc.edu; h.yang@upc.edu

[2]Department of Mathematics, IonSAT, Universitat Politècnica de Catalunya, 08034 Barcelona, Spain; manuel.hernandez@upc.edu ;haixia.lyu@upc.edu

[3]School of Electronic Information and Engineering, Yangtze Normal University, 408100, Chongqing, China

[4]European Commission, Joint Research Centre (JRC), Ispra, Italy

Manuscript received July 19, 2020; revised August 26, 2020.

detected depletion region decreases. This can be interpreted to indicate that the area of the region of relatively high VTEC value increases.

The system for determining depletion regions in the ionosphere has been developed by using GNSS measurements, taking advantage of GIM products of the UPC-IonSAT group that provides real-time GIM maps at a cadence of 15 minutes [*Hernández-Pajares, et al.* (1999)], [*Caissy, M., et al.* (2012)] and [*Li, Z., et al.* (2020)]. The availability of these maps led to the possibility of implementing a depletion detection system based only on real-time GNSS measurements. The algorithm we present, allows us to carry out this process in real-time, with a processing time of the order of 35 milliseconds per map in a standard workstation at the time of writing the article. The links to the real-time product are at Section IX.

The knowledge of the polar electron content depletions can provide the location of regions with higher errors in ionospheric corrections and with ionospheric scintillation and the corresponding degradation of the GNSS, positioning [*Chernouss,S. A., et al.* (2011)].

Real-time detection of regions of depletion services aligns with the Arctic policy [EU Arctic Policy 1 (2020)] published by EC in 2016. There is a growing interest between the EC and the Arctic countries [EU Arctic Policy 2(2020)] and [EU Arctic Policy 2(2020)] regarding the lack of connectivity infrastructure (communication, radar, SBAS/GNSS, mobile, etc.). Moreover, Arctic routes for maritime and aviation are becoming increasingly important, and the real-time depletion detection system could contribute to supporting these developments by providing crucial and specific information focusing on the poles rather than on mid-latitudes.

II. GNSS PROCESS OF THE DATA

The TEC forecasting method relies on time series from the UPC Vertical TEC (VTEC) GIMs (labeled UQRG) computed by TOMION v1 software in the frame of the International GNSS Service (IGS; [*Dow, J. M., et al.* (2009)] and [*Hernández-Pajares, et al.* (1999)]). TOMION is a software mainly developed by one of the authors of this manuscript (MHP) consisting of two main versions: TOMION v1, which is focused on the estimation of electron content models, mostly based on GNSS dual-frequency measurements with ionospheric tomographic and kriging interpolation; and TOMION v2, which consists on a hybrid geodetic and tomographic ionospheric model that allows for precise ionospheric determination and precise positioning, among GPS radio-occultation data processing, see [*Hernández-Pajares, et al.* (1999)], [*Hernández Pajares, et al.* (2000)], [*Orús, R., et al.* (2002)], [*Orús, R., et al.* (2005)]. In particular, either UQRG 15-min resolution with 1-day latency or the UPC real-time VTEC maps (labeled URTG), which are computed continuously at a 30-seconds rate, can be ingested to the forecasting approach. In both cases, the GIMs provide bidimensional VTEC values assuming a thin single-layer ionospheric model at a height of 450 km and considering a world-wide regular grid every 5.0 °/2.5° in longitude/latitude range (i.e., 71 latitudinal and 72 longitudinal points accounting for a total of 5112 VTEC values per map). Note that for building the forecasting time series, these maps are transformed into a local-time sun-fixed reference frame.

In brief, the way to calculate VTEC values in TOMION relies on the simultaneous estimation of the electron density values $(N_e)_{i,j,k}$ of the ionospheric electron content distribution, considering a basis functions of a partition in voxels of indices (i, j, k), and the ambiguity B_I of the ionospheric combination of carrier phases after correcting the small wind-up term ϕ. And both set of parameters are properly estimated without using pseudorange data (i.e. without the need of taking care of hardware code delays, see for instance, [*Wang, et al.* (2016)], [*Zishen, et al.* (2013)]) in a forward Kalman filter solving next equation.

$$L_I - (\lambda_1 - \lambda_2) \cdot \phi = \alpha \sum_{i=1}^{M_I} \sum_{j=1}^{M_J} \sum_{k=1}^{M_K} (N_e)_{i,j,k} \cdot \Delta l_{i,j,k} + B_I$$

Then, each Slant Total Electron Content (STEC, S) affecting each GNSS receiver-satellite signals can be obtained from the estimated carrier phase ambiguity $\hat{B}_I$ as

$$S = \frac{1}{\alpha} \left[L_I - (\lambda_1 - \lambda_2) \cdot \phi - \hat{B}_I \right]$$

Where $\alpha_I = \alpha_2 - \alpha_1 \approx 1.05$ and $\alpha_i = 40.3/f_i^2$. In addition, Kriging interpolation technique [*Orús, R., et al.* (2005)] is used to fill the gaps where there is lack of data, given the inhomogeneous sparsity of GNSS receivers, as the last step of the TOMION processing chain to derive UPC GIMs [*Feltens, et al.*(2011)], [*Hernández Pajarez, et al.* (2016)].

The results presented in this work have been obtained from UQRG maps since these have proven to have the best performance against independent TEC measurements - JASON test - from altimeter data, as well as independent GNSS receivers -dSTEC test- among the different IGS models (for the details, see [*Roma-Dollase, et al.* (2017)]). In particular, the results from this paper have been derived from UQRG data in years 2014 -coinciding with the mild 24^{th} Solar Cycle maximum-, 2015 and 2016.

III. CRITERIA FOR SELECTING THE TEST DAYS

The criterion for deciding the examples to test the method was to use a) maps of extreme depletion (i.e. troughs) reported in the literature, and the temporal context of the events and b) examples either of the other pole (different season) or near day without storms. In particular we selected the following works; [voiculescu (2016)], [karpachev (2019)], [Shinbori(2018)] and [Zou (2011)] which analyse by different methods the presence of ionospheric troughs. In Table I we present a summary with the dates, values of measured VTEC on our maps and solar cycle, and the reference to the papers in the literature that analyse the events.

There polar depletion or troughs that we will use as benchmarks were established by different methods such as: GNSS [Shinbori(2018)], [Karpachev (2018)], Radar [Shinbori(2018)], [karpachev (2019)] and Ionograms from satellites [Shinbori(2018)], [karpachev (2019)], [Karpachev (2020)].

IV. Image segmentation as a tool for determining Polar Depletion regions

The method for finding the depletion regions in the Polar Ionisation maps consists of image processing tools. To achieve this, we will make an analogy between polar VTEC maps and greyscale images. The process consists of a first part of image enhancement followed by an image segmentation method that is suited to how the ionization regions in the polar region manifest themselves.

The proposed method determines a depletion region, along with intermediate and high ionization regions. One aspect of the method that should be highlighted is that by taking advantage of the properties of the morphology of the ionization regions, the results are quite independent of the initial thresholds for determining the depletion regions. This independence of the thresholds is determined by the nature of the method, which is based on an analogy to geological landscapes, i.e. geological surface analogy is determined by the gradient of the VTEC map, and a flooding analogy where the flooding process that arises from the lower regions, i.e., initial depletion region determined by a threshold.

The procedure that we propose has two components,

1) the first consists of an enhancement of the VTEC maps (i.e. equalization of histograms, see section VI), which is a technique that increases the contrast in the images, to allow that by simple visual inspection one can determine with greater clarity the depletion areas. This process creates a new image with a different scale of values, which increases the contrast of the image, and therefore makes it possible to better determine the regions that make up the image.
2) the second one of segmentation (watershed segmentation see section VII), which determines the regions through a physical analogy to the watershed boundaries determined by flooding. In this analogy, the gradient of the VTEC value (grey level) acts as an altitude and thus the map becomes a topographical surface.

The two techniques are linked, as the enhancement of the image allows to produce basin boundaries, which determine regions of uniform VTEC, and the most significant feature; provides a barrier between regions that follow the shape of the ionization patterns.

V. Selection of the segmentation method

The idea underlying the paper is finding the depletions employing a segmentation method. In a preliminary study, we tested several types of segmentation methods. The initial problem we encountered was that there is no clear criterion for defining a depletion. Therefore the preliminary analysis consisted of searching for a method that could be adapted to the problem. Another relevant requirement is that we did not want to tailor the method to the examples at hand, hence the need for a method that should be natural and flexible to the level of the thresholds. The trainable segmentation methods based on labeled samples were not suited because the number of depletions/troughs detected independently using radar, satellites, etc., is limited. This rules out approaches such as clustering methods, based on thresholds such as Otsu's and histogram-based methods. (for a description of these techniques, see for instance [Gonzalez(2007)]).

Another type of segmentation approach is based on Mathematical Morphology. These methods work basically with binary images and with grayscale images. As for the Mathematical Morphology methods based on grayscale, we considered Morphological Snakes [Marquez-Neila(2013)], which find level contours. This approach is well suited to the type of problem we want to solve. This technique resulted in a large number of regions, and we could not find a criterion to separate the depletion zones from the false alarms.

An alternative segmentation method consists of graph partitioning via 'min-cut' criteria. These methods rely on creating a distance graph and decomposing the adjacency matrix into eigenvectors. This type of method leads to spurious segmentations when the criteria for filtering distances create subgraphs of a very unbalanced size. One correction is the normalization of the slices (see [Shi (2000)]). However, with polar VTEC maps, where there are regions with little VTEC variability, this method was unable to detect the depletions.

The watershed segmentation method gave a good performance, with a low degree of dependence on threshold levels. This method fits naturally to GIM maps, and which we described in the section VII.

VI. Justification of the histogram equalization as preprocessing step

Histogram equalization is a tool for changing the values of the pixels of an image to generate a new image with a higher contrast (see for instance [Gonzalez(2007)]). In Appendix A, we present a summary of the histogram equalization method for images. The lower left figure is the histogram of a polar ionization map normalized to the maximum VTEC value. The distribution of VTEC values is more frequent in the lower range, i.e., the range of values that comprise most of the observations is around the interval 0.1 to 0.35. The equalization process expands this range and assigns the VTEC values in this range of about $0.1, 0.35$ to a range of about $0.1, 0.65$. The result is that the set of most common values is spread over a larger margin, increasing therefore the resolution associated with the VTEC values that occupy most of the area of the Polar Map.

The effect of equalizing the histogram is shown in two different cases in Figures 5 and 18, the upper row left: original map ,upper row middle: map after equalization. The orange dot is the location of the minimum VTEC value. Note that as the contrast in the image has increased and the borders between regions are more clear. This makes it easier to locate the depleted regions and thus have a qualitative idea of the area of the map's regions.

The gradient of the equalized map fits the way the segmentation algorithm used to detect the depletion region works. The equalization creates more uniform regions with clearer transitions between regions. When computing the gradient, this results in the presence of barriers between uniform regions. (see for instance Figures 5 and 18 upper row right). The consequence is that the border between areas of different ionization

is emphasized. This allows the segmentation algorithm to find regions of uniform ionization rather than independently of the initial thresholds.

Note that an alternative to the global histogram process described in Appendix A is the local histogram equalization [Gonzalez(2007)], which consists in equalizing locally the histogram. In section VII, we note that to be able to segment the Polar maps and determine correctly the location of the depleted regions we need an operator that determines the borders between regions. The gradients associated with the original images (i.e., without equalization) gave poor boundaries between regions. Also, the use of the local equalization due to the local nature of the process blurs the boundaries and hence the gradient of the map gave less information about the homogeneity of the regions. This fact was also empirically confirmed, and therefore we discarded the use of a local histogram.

VII. Description of the watershed segmentation

The segmentation method relies on an analogy with geological basins that separate neighboring drainage regions. In this analogy, the gradient of the VTEC values will correspond to altitudes and thus can be considered as a topographical surface. The drainage boundaries appear from the local gradient because the areas of high variation of the VTEC (gradient in high absolute value) correspond to what would be natural boundaries between regions of interest, and the areas of almost constant VTEC (gradient in low absolute value). The boundaries of the related regions of interest in the segmentation will be determined from a flow that will emerge from tagged points. The algorithm is called watershed due to the analogy mentioned above, was proposed initially by [Beucher (1979)], and the form in which it is applied in this paper follows Meyer [Meyer (1992)]. The implementation (see [Van der Walt(2014)]) used in this paper corresponds to the variant described in [Neubert(2014)].

The flow from the labeled points (i.e. percentiles of amplitude on the processed map $< 1\%$, 10% and, 60%) is guided by the contours defined by the gradient. Examples of the contours and their relation to the equilibrium flow can be seen in the figures in the results section VIII.

To determine the regions of interest we implemented the seeded watershed segmentation or marker-controlled watershed where the algorithm is initialized by labeling certain parts of the map and a queue-based algorithm expands the pixels related to the labels following the flooding analogy. In our case the initial labels were the following:

- Depleted region: pixels with the VTEC percentiles $< 1\%$.
- Intermediate Ionized region: pixels with the VTEC percentiles between 10% and 60%.
- High Ionized region: pixels with the VTEC percentiles $> 60\%$

The selection of thresholds as discussed in Section IV is not unique and with differences around the values, we propose to give similar results. The thresholds determine points from which the segmentation grows, following the contours defined by the gradient of the image with the histogram equalized. The equilibrium point determines the borders. As we have been able to verify empirically, the final result is quite insensitive to changes in the levels we propose. The thresholds express the qualitative difference between very low ionization value, medium value, and high value.

We have intentionally defined the thresholds in the form of a percentile, to make the algorithm independent of ionization levels and the solar cycle. Besides, the values we have chosen for the thresholds are justified because the depleted region must have labels corresponding to the lowest values, which in our case we decided on 1%. Since the algorithm expands regions using the flood metaphor, we leave an unlabeled region between 1% and 10%, so that the boundaries depend more on the shape of the gradient than on the chosen thresholds. On the other hand, it was arbitrarily decided that the region with the highest 60% ionization was the upper zone. Leaving a free region between 1% and 10% is justified because the depletion region shape is not well defined, in the sense that the VTEC values and reasons for depletion are multiple and correspond to different origins. Deciding the thresholds between 1% and 10%, gave the algorithm flexibility in assigning the area to the depletion zone as can be seen for instance in Figure 4 left, where we plot the evolution of the depletion area as a function of the time and varies from a 1.4% of the map to 9.7% (the total area of the map is $74.70\times10^6 km^2$). An interesting feature of the algorithm is that changing the middle threshold, from 10% and 20%, gave just a small increase in the area of the detected depleted regions, albeit biased towards the equator.

The working principle of the algorithm is based on having a few labeled pixels and increasing iteratively pixel by pixel the region associated with each labeled pixel until the border around another label is reached. The direction (or flow) of the growth of the regions is determined by the borders given by the image gradient. Note that in the metaphor of the algorithm, the flow can be directed upwards from the 1% labels or downwards from the 10% labels. The algorithmic details are explained in the references [Meyer (1992)] and [Neubert(2014)].

In Figure 1 we show three examples of how the points labeled as 1% and 10% give rise to the depletion region. These correspond to maps for different dates where different authors reported troughs (i.e., regions of high depletion). The upper row shows the initial labels on the VTEC maps, the lower row to the depletion partitions determined by the algorithm:

- (upper row) Ionization percentile: light blue $< 1\%$, yellow between 10% and 20% and red $> 60\%$. The dark blue is the free region.
- (lower row), Regions determined by the algorithm: light blue depleted region, yellow medium ionization, red high ionization.

The bottom row shows the result of the growth determined by the gradient-guided flooding. The dark blue dot in the depletion region corresponds to the coordinates of the lowest VTEC value of each map. As the algorithm works following the metaphor of a flood, the shape of the barriers given by the gradient combined with the distance to the seed points can potentially give rise to highly irregularly-shaped segments. When comparing the depletion regions with the gradient maps

it is important to keep in mind that the initial seeds ($< 1\%$ marked in light blue in the upper row) are distributed within a very small region. Also as can be seen in the Figure, there is a tendency to create compact regions.

A detailed account of how the algorithm works in a concrete case (2017/94 at 06:00 (UT), Figure 5) is explained in Section VIII-B.

VIII. Results

In this section, we will check the performance of the algorithm for detecting Polar Depletion regions using as benchmark three articles that report the presence of Polar Troughs. We define the polar regions on which we have computed the results as the regions comprised between the latitudes [45° to 90°] and [-90° to -45°]. The intervals were decided to avoid missing the border of the depletion regions and other polar features.

The experiments were programmed in python, and the image processing libraries used were the scikit-image [Van der Walt(2014)]. The processing time was of 35 milliseconds per map in a standard desktop computer (Intel i5).

In this section, we will begin with a general description of the VTEC statistics of the days selected for testing the algorithm, followed by a detailed analysis of each of the days with confirmed troughs. Given that the troughs correspond to moments of high depletion, with these examples we can characterize the properties of the algorithm in terms of detection of these events, and the temporal evolution of the depletion zones in the course of the day.

A. Statistical description of the days analyzed

In this section we will summarize the properties of the VTEC in the maps studied in the next subsections.

A first summary of the VTEC distribution is shown in Figure 2. This Figure depicts the box plot distribution of the VTEC values for the events of extreme depletion mentioned in the analyzed paper. Note that the events are labeled by the date and refer to specific timestamps in the day, such as the time a trough was reported. The central box indicates the limits from the lower 25% percentile to the 75% percentile. The ranges of variation follow the solar cycle, and several outliers appear (shown with circles).

In the Table I we present a summary of the characteristics of each one of the events, with information of the minimum VTEC value, the average VTEC value within the detected depletion zone (about two standard deviations higher than the minimum value) together with the standard deviation (in the order of 1/5 of the average value), the average value of VTEC outside the depletion zone with the standard deviation (in the order of 1/2 of the average value), together with the detected depletion % area (% over the area of the map $74.70\times10^6 km^2$), and the solar cycle.

The VTEC distribution shown in Figure 2 is complements the summary shown in Table I, in which the values have been differentiated within (first two columns) and outside the detected depletion region (third column). An interesting aspect is that from the table one can observe that the mean value within the depletion zone plus the standard deviation of the VTEC in this zone is in all cases below the 25th percentile of the VTEC distribution for the whole map as seen in Figure 2.

Figures 4, 7, 11, 17, 19, 21 show for different events, the result of applying the algorithm throughout the day at time intervals of 15 minutes. In the figures, we overlay, the average VTEC values inside and outside the depletion zone and the area occupied by the depletion region. A common issue to all time series is the fact that the minimum VTEC value and the average values inside and outside the detected depletion region change slowly during the day, and do not show important changes in the time intervals in which the trough is reported. Note that in these plots we did not low pass filter the estimated values to show the properties of the algorithm concerning outliers. In a real-time application, a smoothing of the time series might have sense.

While the RMS error of the UQRG model is better than that of other GIM models, the TEC of the polar region is lower than that of the middle and low latitudes. An objection to the use of this model, might be that the relative error of the model is larger in the polar regions. Nevertheless, as shown in [Hernandez (2020)], (Figure 2 of the same article) can be seen as a typical standard deviation of UQRG VTEC vs. altimeter VTEC of less than 2 TECU in North high latitudes from 2002 to 2018. On the other hand in Figure 14 (of the same article), the smallest value of North High Latitude VTEC is larger than 2 TECUs, ranging up to more than 25 TECUs during the same period longer than one solar cycle, including the case studies in the present manuscript.

As for the South Pole, despite the number of GNSS receivers is smaller in Antarctica, the worsening of the UQRG GIM performance is just 0.5 TECU in the most frequent values by comparing the same validation vs. altimeter measurements (compare Figures 3 and Figure 2 of [Hernandez (2020)]). And the lower mean values are at similar levels, ranging above 2 TECU, and with the higher values still larger at South High Latitudes.

In the next subsections, we will study each of the reported days individually.

B. Polar Depletion corresponding to the 2017/94

In this section, we will analyze the Geomagnetic Storm Event on 4 April 2017. This event was studied in detail by [Shinbori(2018)] using information from GNSS, radar, and the Arase satellite. In the cited paper, they use the Arase satellite to analyze the plasma wave dynamic spectrum data provided by the High-Frequency Analyzer, which is a subcomponent of the Plasma Wave Experiment onboard the Arase satellite used to identify the upper limit frequency of upper hybrid resonance waves along the satellite orbit. In the paper, the authors also checked the results employing the SuperDARB radar.

The authors of the paper studied the temporal and spatial variations of the mid-latitude trough in the ionosphere. To determine the position of the trough event, the authors computed the overage GNSS-TEC grid data of 10 geomagnetically quiet days in April 2017, which was subtracted from the storm time GNSS-TEC measured every 5 minutes. The location

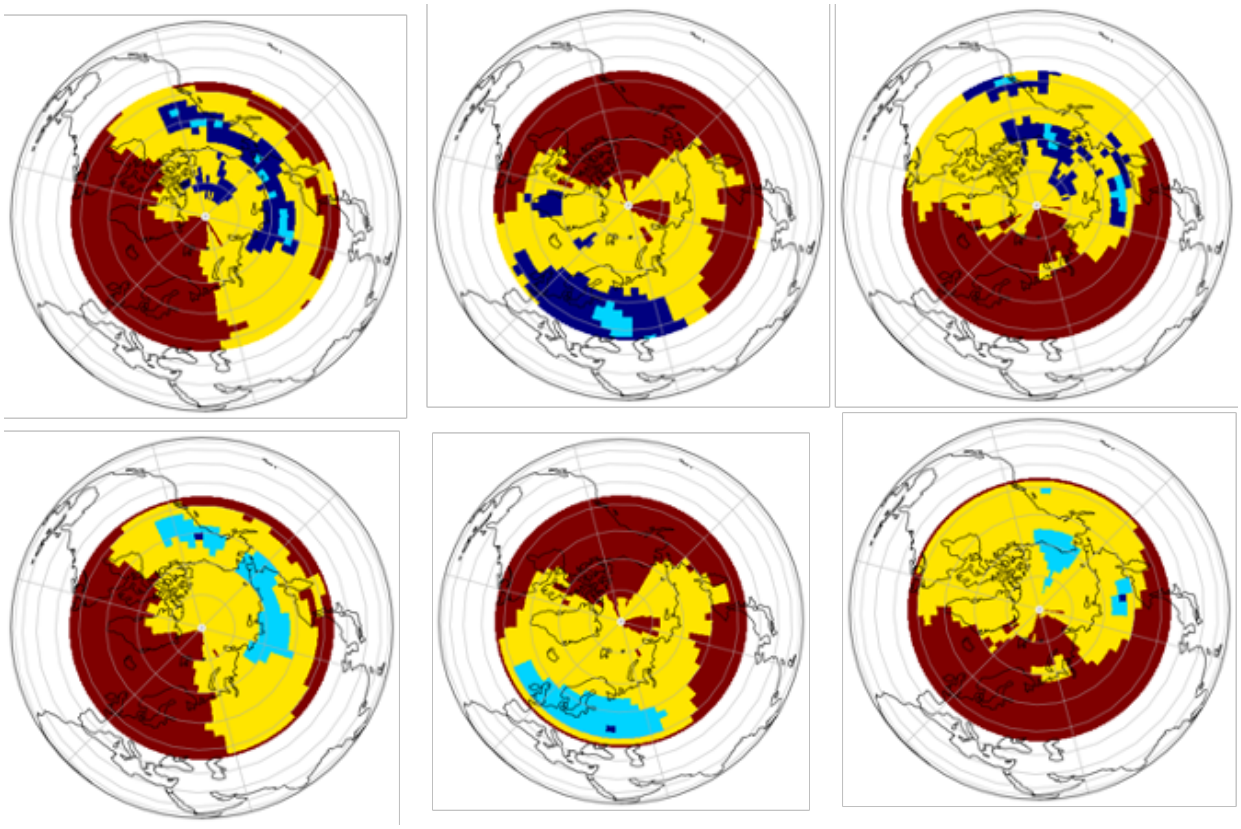

Fig. 1. Upper row: initialization of the algorithm. Lower row: Depletions detected after the watershed algorithm corresponding to three case studies. Left column: [Zou (2011)]. Middle column [voiculescu (2016)]. Right column [Shinbori(2018)].

TABLE I
SUMMARY OF THE VTEC IN/OUT THE DEPLETION REGIONS, % AREA, REFERENCES TO SECTION AND BIBLIOGRAPHY.

Year/Day (Time)	Min. VTEC	Mean(σ) VTEC In Depletion	Mean(σ) VTEC Out Depletion	Depletion Area	Solar Cycle/activity (hemisphere)	Sect.	ref.
2001/051	6.8	10.76(1.3)	29.7(11.6)	8.7%	23/high (South)	VIII-C	[karpachev (2019)]
2004/138 (08:30 UT)	4.8	5.0(0.1)	15.1(7.6)	1.7%	23/low (North)	VIII-D	[voiculescu (2016)]
2004/138 (22:30 UT)	8.6	11.5(1.7)	18.1(5.6)	7.0%	23/low (North)	VIII-D	[voiculescu (2016)]
2004/138 (23:45 UT)	8.8	11.6(1.5)	17.9(6.3)	7.6%	23/low (North)	VIII-D	[voiculescu (2016)]
2007/210	4.3	1.09(0.2)	2.96(3.6)	5.1%	23/low (South)	VIII-C	[karpachev (2019)]
2007/285	1.9	2.7(0.1)	6.4(2.5)	6.9%	23/low (North)	VIII-E	[Zou (2011)]
2008/068	1.2	1.9(0.1)	6.1(2.6)	2.3%	23/low (North)	VIII-E	[Zou (2011)]
2017/094	2.3	3.7(0.1)	8.7(5.1)	2.9%	24/med (North)	VIII-B	[Shinbori(2018)]

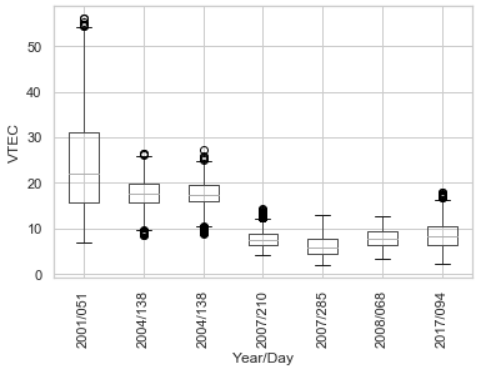

Fig. 2. Box plot diagram of the distribution of the VTEC for the maps studied in this paper

of the trough was obtained after a low pass filter using a boxcar window of $1.5° \times 1.5°$, followed by a keogram at each longitude. The trough minimum in the paper was determined by the position of the minimum value of the GNSS-TEC in each keogram.

One of the properties of the segmentation method that we propose is that it does not use past values to determine thresholds, but VTEC quantiles are in a GNSS map. Also, as no spatial low pass filter is applied, arbitrary shapes of the depletion can be detected, including the possibility of disconnected depletion regions.

As an example, in Figure 3 we show the evolution of the detected depletion regions in the time interval from 4:30 (UT) to 10:00 (UT). The geographic coordinates of the minimum VTEC value are marked with a dark point within the region in blue. An interesting aspect of the event is that at the time the

trough is reported [Shinbori(2018)] (06:30 UT), the area associated with the depletion region drops suddenly and increases slowly afterward giving rise to disconnected depletion zones. Another example of the disconnected depletion zones related to this event is shown in the rightmost column of Figure 1. The origin of this disconnection, (see Figure), originates from the presence of a high ionization ridge in between the two regions of extreme low ionization.

The temporal evolution of the VTEC values inside and outside the detected depletion region together with its area is depicted in detail in Figure 4. This figure shows clearly the oscillation of the area of the detected depletion region at the time surrounding the reported trough event. In line with the area of the depletion region, there is a sudden change in the latitude of the minimum of ionization. The minimum value of the depletion area occurs around 6:30 (UT), as mentioned in [Shinbori(2018)]. Besides during the storm, there appear four other moments of minimum area. Another feature is that the minimum VTEC value increases suddenly after the onset of the storm but in contrast the mean VTEC value in the depleted area increases in a smaller amount. We have found that the troughs mentioned in [Shinbori(2018)] correspond to regions of a small area but are not associated with a pronounced decrease in the VTEC value. That is the global mean outside of the depletion region increases as the area of the depleted region decreases.

The evolution of the Polar maps shown in Figure 3 is consistent with the results in [Shinbori(2018)], where the authors state that after the onset of the geomagnetic storm, the trough minimum location moves equatorward from 60° to 48° within 4 hr which corresponds to 8:00 (UT) (see the time evolution of the latitude of the minimum VTEC in Figure 4 right). The algorithm finds three unconnected depletion regions, being the deepest the one at 48° which is the border of the map. The authors in [Shinbori(2018)] state that the equatorward movement implies a shrinking of the plasmasphere due to an enhanced convection electric field in the inner magnetosphere associated with the geomagnetic storm. Also, the article characterizes the intervals before the storm (04:00(UT)), within the storm (06:00(UT)), peak (8:00(UT)) and the recovery phase (11:00 (UT)), relating it to solar wind measurements, IMF and SYM-H index. The intervals mentioned in the article coincided with the time intervals in which the area of the detected depletion zone oscillates sharply, reaching several minima as seen in Figure 4 left.

In Figure 5, we show the results of applying the algorithm to a GNSS Polar Map, measured at the reported moment of maximum depletion at 06:00 (UT). The location of the point of maximum depletion is marked in light at the two upper left maps, and in dark at the lower left-map. The result of equalizing the initial GNSS Polar map emphasizes and makes more clear the different regions of ionization. The map corresponding to the spatial gradient (upper right) shows areas where the ionization has a constant value (dark blue), and areas where there is a rapid variation (red and green). Note that the light green part, which corresponds to slight variations in space of the VTEC value, occurs mainly in the low-ionization zone. These regions of change in the VTEC control the change/flow of area in the watershed algorithm. This aspect of the spatial gradient allows us to distinguish the structure of large relative depletion zones within the low-ionization region. The segmentation algorithm assigns the low/medium/high ionization labels according to the percentile ionization thresholds. Thus the region of the lower 1% ionization will increase flowing to the higher ionization zone through the non labeled region, and from the 10% ionization labeled region, the region with this label will flow to the lower ionization zone also through the non labeled area. That is, the process consists of conducting the flow of the region from the low tags to the high tags and vice versa through the intermediate zones, controlling the process through the gradient profile of the equalized map. When equilibrium is reached, a partition of the map shown in the lower left is created and displayed in light blue. One issue to highlight is that the intermediate region (non labeled) between the 1% and the 10% labeled points, as shown in Figure 1, usually surrounds the bottom 1% irregularly and is small in area. This is compatible with having a moderate gradient in the regions of minimal ionization since from these zones the ionization value can only grow.

The detection of the depletion zone is made by expanding the zones with an ionization value of less than 1%. This effect can be seen in the two map views shown in the Latitude/Longitude vs. VTEC figures at the bottom right. Note that VTEC values surrounding the minimum region the ionization increase. That explains why the gradient in the zone associated with the depletion is different from zero and why it serves as a structure that guides the flow that determines the depletion region.

Note that the moment that the trough is reported at 6:30 (UT) is also the moment of maximum intensity of the geomagnetic storm and coincides with the minimum area of the depleted regions as shown in Figure 4.

C. Polar Depletion corresponding to 2001/051 and 2017/210

In this section, we study two events reported in [karpachev (2019)], corresponding to the days 2001/051 and 2017/210. The examples in this section differ from the others in that they deal with the South Pole (vs. the North Pole) and have a medium/high solar activity (vs. low). Furthermore, given that the density and distribution of stations at the South Pole is different, we will be able to appreciate the effect of reducing the number of stations.

For comparison purposes, we will present the depletion zones determined for the same day at the two poles. This will allow us to see how the algorithm works in conditions of complementary seasons, and different states of the ionosphere.

The authors in [karpachev (2019)], when justifying the form of depletion, speak of walls between regions of the ionosphere. This metaphor fits the way the algorithm determines the depletion regions. They also report observational data for the days selected for this study gathered by in-situ measurements of N_e at heights of 330-475 km on board the CHAMP satellite for the years 2000-2009 during low, moderate and, high solar activity. These days had a the quiet geomagnetic conditions, $K_p = 2+$ for $2001/051$ and $K_p = 1$ for $2007/210$.

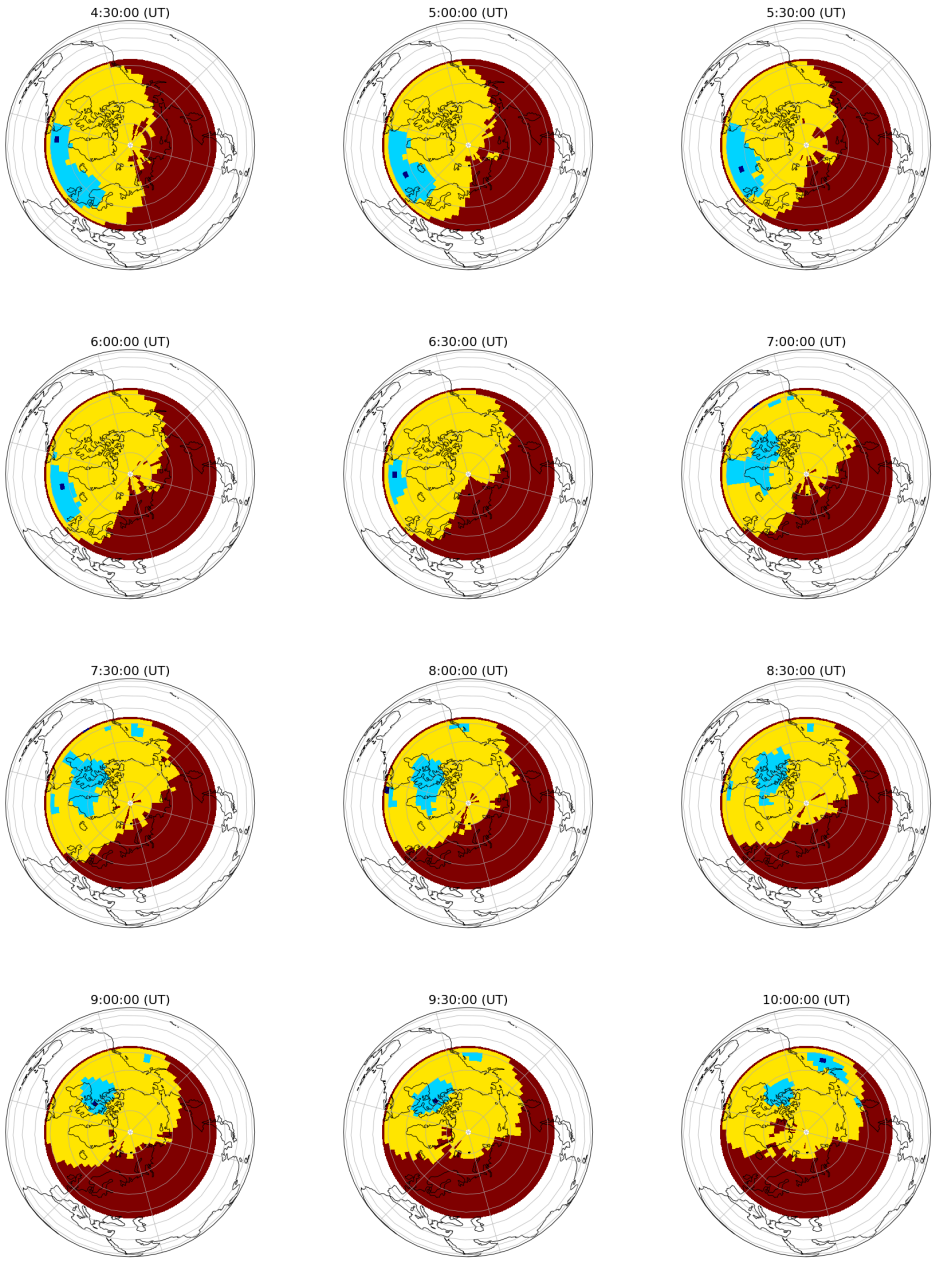

Fig. 3. Sequence of maps at day 2017/94, showing the depletion location.

To facilitate the reading of the section, in Table II we present the dates, time and, season of the examples studied.

TABLE II
MAPS ANALYSED IN THIS SECTION.

Year/day	Time	Figure number
2001/051	North Pole 22:30 (UT) Winter	6
2001/051	South Pole 22:30 (UT) Summer	8
2001/051	North Pole VTEC Time evolution	7
2001/051	South Pole VTEC Time evolution	9
2007/210	North Pole 13:45 (UT) Summer	10
2007/210	South Pole 13:45 (UT) Winter	12
2007/210	North Pole VTEC Time evolution	11
2007/210	South Pole VTEC Time evolution	13

We selected the days were the author report the presence of a trough at the North Pole (Figure 6) and at the South Pole (Figure 12) . For comparison purposes, we show the complementary Pole maps, where no presence of troughs was reported (see Figures 8 and 10).

The troughs reported in [karpachev (2019)] coincide in time and position with the regions of depletion found by the method proposed in this paper. The authors report (Figure 1 of [karpachev (2019)]), for the day 2001/051 the presence of two minima of ionization (measured by f_p) located in the latitudes 75° and at about 60°. Our method also detects one of the minima at approximately about 63° as shown in Figure 8 (lower middle). (Note that as in our case the measurements

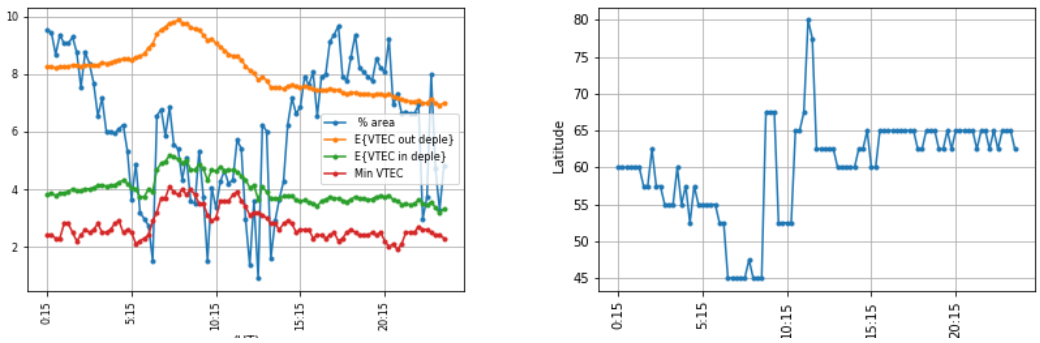

Fig. 4. Day 2017/94 . **Left**: Blue: % of the area of the detected depletion. Red: minimum the VTEC in the depleted region. Green): mean value of the VTEC in the depleted region. Orange: mean value of the VTEC out of the depleted region. **Right**: trajectory of the latitude of the minimum VTEC value along time.

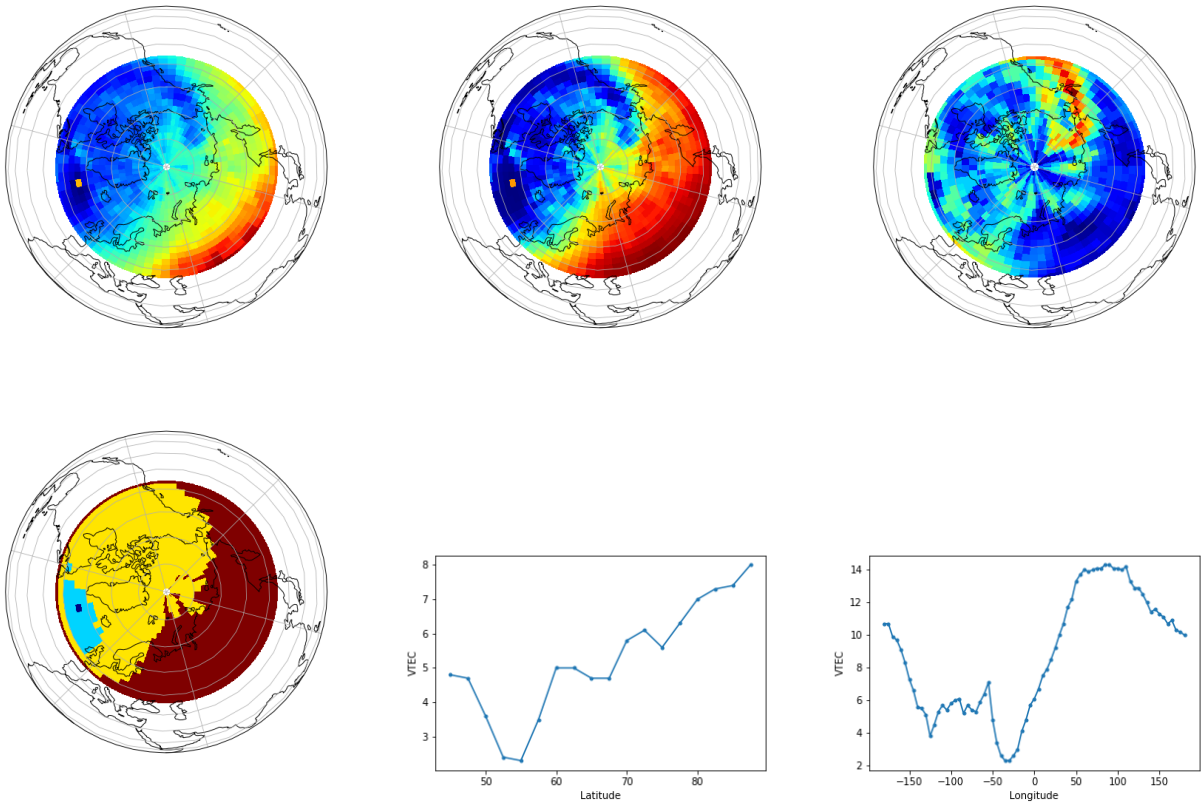

Fig. 5. GNSS Polar Map 2017/94 at 06:00 (UT). Upper left: VTEC map, Upper middle: after equalization. Upper right, spatial gradient of the original VTEC map. Lower left: detected depletion in light blue. Lower middle: Latitude vs. VTEC. Lower right: Longitude vs. VTEC.

are done over GNSS the VTEC vs. Latitude plot is smoother). The minimum located at 75° can be seen in the maps of the upper row for a Longitude about 100° degrees. The trough at 75° is not detected by the algorithm, because it is a depression located in a medium/low ionization region, with a higher ionization level than the region detected as depletion.

For the observation at day 2007/210, the trough is located at the south pole, and the authors report a local minimum at about 77° which corresponds to the minimum VTEC shown in Figure 12 (lower middle).

In figure 6, we show the result of applying the algorithm to the North Polar GNSS map at 2001/051 22:30 (UT). In the upper left, we present the measured GNSS map, and in the upper middle, the result of equalizing the VTEC distribution. By equalizing the distribution of VTEC levels, the regions of high, medium, and low ionization are better delimited, and therefore the areas with uniform ionization in space are better defined. Hence the spatial variation of the ionization results in structures that follow the boundaries in different ionization regions and at the same time detect the zones of change of the ionization around the minimum ionization.

The algorithm takes advantage of both features of the

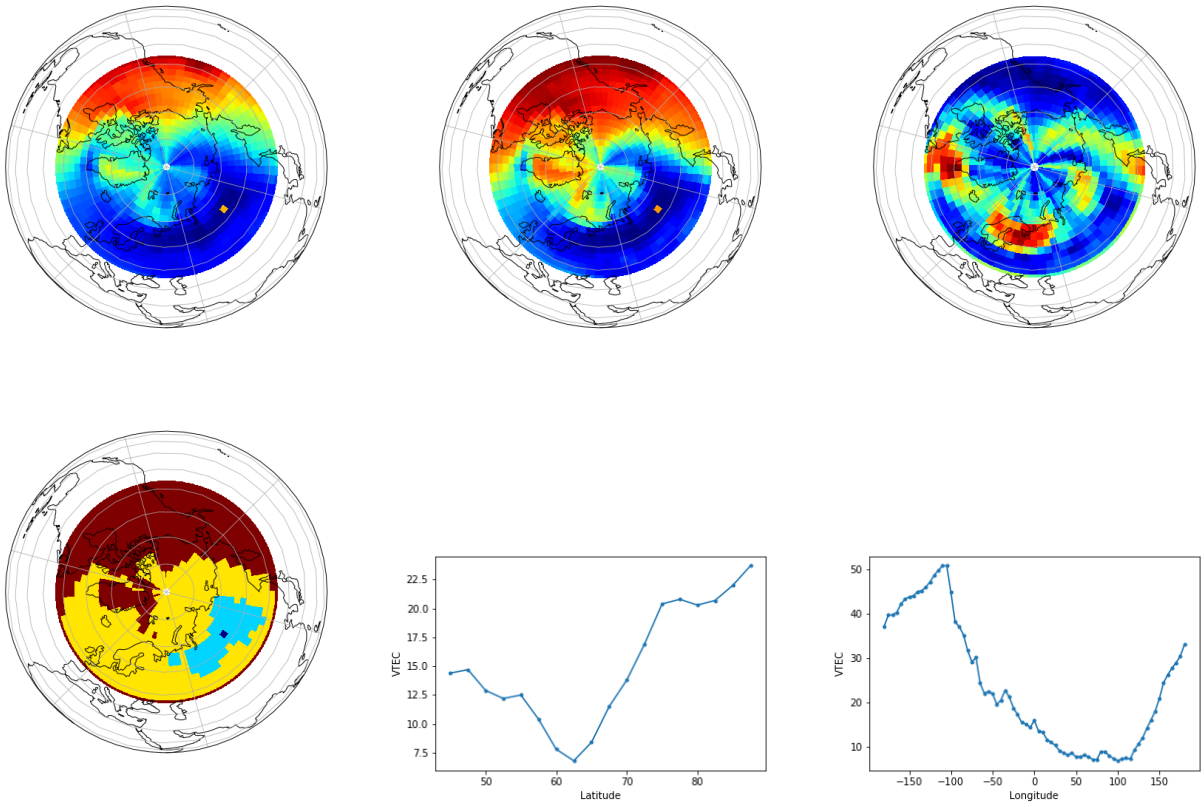

Fig. 6. North Pole GNSS Polar Map 2001/051 at 22:30 (UT) (Winter). Upper left: VTEC map. Upper middle: equalized map. Upper right, spatial gradient of the equalized map. Lower left: detected depletion in light blue. Lower middle: VTEC vs. latitude. Lower right: VTEC vs. Longitude.

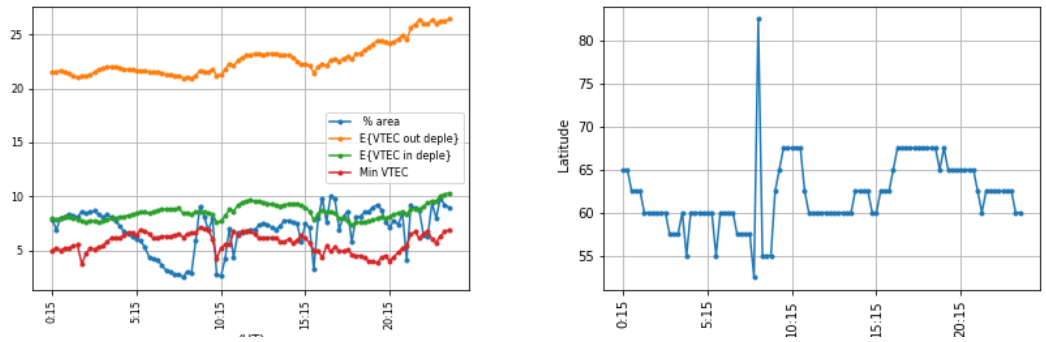

Fig. 7. North 2001/051 **Left**. Blue: % of the area of the detected depletion. Red: minimum VTEC in the depleted region. Green: mean value of the VTEC in the depleted region. Orange mean value of the VTEC out of the depleted region. **Right**: the trajectory of the latitude of the minimum VTEC value along time.

gradient because it provides for the regions that are initially marked as corresponding to the lowest 1% of ionization the following information:

- an indication of the directions of growth (note that the gradient is high around the minimum indicated with the light orange point)
- the walls between regions of uniform ionization with different levels (observe that the gradient creates spirals that go to the north pole), allows redirecting the flow or increase of area in the non labeled regions between the region of low ionization (i. e. $< 1\%$) and the medium ionization region (i.e., $> 10\%$).

The algorithm's output is shown in the lower-left figure, where the contours of the depletion region are clearly marked. The ionization in the detected depletion region is not uniform, as shown in the two figures in the lower row. The VTEC value varies in the latitude direction between 7.3 and 11 TECUS, while in the longitude direction the variation is more flat and asymmetric around the minimum.

In Figure 7 we show the temporal evolution of the area, VTEC, and latitude parameters of the minimum position. The temporal evolution of the estimated parameters is smooth. It

should be noted that the time evolution of the VTEC minimum value in the map is relatively independent of the area of the detected depletion and that at the moment the trough is reported the only significant change was a slight decrease in the latitude of the minimum ionization.

In Figure 8 we show the result of applying the algorithm to the map corresponding to the south pole, where [karpachev (2019)] do not report the presence of troughs. For comparison purposes, we selected the same day and time. In this case, the maps are smoother due to the presence of fewer stations. The result of the equalization showed a smooth variation between the high/low ionization regions. The detected depletion region is flat in terms of VTEC and the Latitude/Longitude vs. VTEC plots shown in the lower row of Figure 8 show that the VTEC in the depletion region is about 2 to 3 times lower than the value outside.

In Figure 9, we show the temporal evolution of the parameters that describe the depletion regions and the only remarkable feature is that the latitude of the minimum of VTEC moves suddenly to the equator and stays for about one hour at latitude -85° degrees, returning afterward to -57° degrees. Note that the sudden changes in the latitude of the minimum VTEC value coincide with sudden changes in the values of the VTEC in the depletion region and oscillations in the depletion region area. Besides, the VTEC values follow the day cycle, and the minimum value is practically identical to the average value in the depletion region from 11:00 (UT). This indicates that the variability within the depletion region.

In the example of day 2001/051, the North Pole map (winter) and the South Pole map (summer) show different patterns. The differences consist in the fact that the distribution of VTEC values (minimum value, average value within the depletion zone, average value outside, together with the area of the depletion zone), have different ranges of variation. While in both Poles the overall average value of VTEC is similar (south pole 1.3 times greater than the north pole), the differences in the VTEC within the depletion zone are much greater, up to 2.5 times greater at the maximum. On the other hand, the VTEC distribution follows the day pattern in the summer hemisphere. Around the time the trough is reported, there is an increase in the area of the depletion region, along with an increase in the level of ionization inside and outside the depletion region.

Next, we will study the 2007/210 event. Concerning the previous case, the seasons are reversed, i.e., the north plot will be in summer and the south in winter. On this date, [karpachev (2019)] reports the trough at the South Pole. As a comparison, we will study the depletion at the north pole coinciding in time, and we will also show the temporal evolution during the whole day of the depletion area and the associated VTEC values.

Figure 10 shows the North Pole map at 2007/210 at 13:45 (UT). After equalization, the high, medium, and low ionization regions are better defined. The spatial gradient of the equalized image highlights the zones of high change. These zones appear as walls between the regions with different ionization levels and also highlight the presence of small amplitude variability in the region adjacent to the minimum. The algorithm determines a depletion region, with the minimum VTEC value located at the border. This can be seen in the latitude vs. VTEC plot, which shows a sudden increase in the VTEC level near the minimum.

The temporal evolution of the VTEC distribution (Figure 11) shows that the area of the depletion decreases significantly between 4:00 (UT) and 11:00 (UT), which coincides with a shift of the latitude of the VTEC minimum from 60° degrees to 47°, returning to 57° degrees at the time when the area of depletion increases. The average value of VTEC within the depletion area drops by half in the time interval when the depletion area is minimal, while the minimum VTEC value barely changes in this temporal interval. On the other hand, the average value of VTEC outside the depletion region does not vary throughout the day.

In Figure 12 we show the map corresponding to the trough reported in [karpachev (2019)] at 2007/210 13:45 UT. In this case, the use of equalization highlights the differences found in the low-ionization zone, which originally covers almost the entire map. When applying the equalization, the presence of two low-ionization zones is emphasized, and in the case of the detected trough, the spatial gradient encircles the depletion region.

The maps and the longitude/latitude vs. VTEC plots show that the minimum ionization is located at the border of the depletion region. In the figure relating VTEC to latitude, an abrupt growth of the VTEC level appears neighboring the minimum. The detected latitude of the minimum VTEC coincides with that reported in the article cited above. Note that the detected depletion zone has a triangular shape that follows the contours of the gradient which in turn exhibits a spiral shape oriented towards the pole.

The time series shown in Figure 13 shows a smooth trajectory of the VTEC in the two regions. The average value of VTEC in the area outside the depletion is almost constant, being twice the minimum value. In turn, there is little variation within the depletion region, as the minimum VTEC value almost coincides with the average value within the depletion zone. Note that the latitude associated with the lowest value shows a significant fluctuation. A plot (not shown in this paper) of the maps at 15 minutes interval for this day (i.e., similar to Figure 3) showed that the morphology of the depletion region changes fast, but the overall trajectory is smooth. This leads us to think that an improvement of the system would be to use the center of masses of the depletion region instead of the latitude of the minimum VTEC value. This center of mass would be a better indicator of the position of the depletion.

A feature of the temporal evolution of the VTEC values is that a minimum appears practically equal to zero towards 3:30 UT, which coincides with a drop in the depletion area and an abrupt change in the latitude of the minimum towards the pole. A similar situation occurs from 22:00 UT when the minimum VTEC value returns to almost zero and the latitude minimum VTEC value drifts slowly to the Pole.

D. Polar Depletion corresponding to the 2004/138

In this section, we will examine two midnight troughs reported by [voiculescu (2016)], (May 17, 2004, at 22:00 and

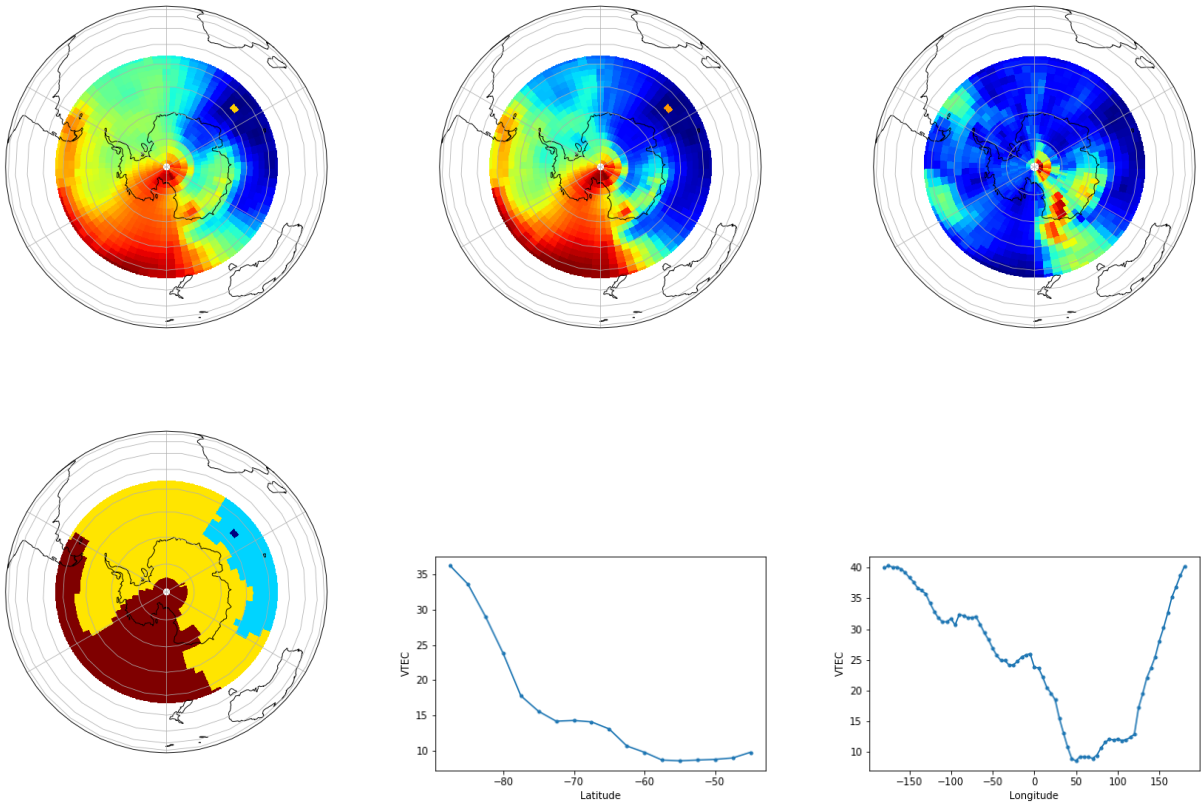

Fig. 8. South Pole GNSS Polar Map 2001/051 at 22:30 (UT) (Summer). Upper left: VTEC map. Upper middle: equalized map. Upper right: spatial gradient of the equalized map. Lower left: detected depletion in light blue. Lower middle: Latitude vs. VTEC. Lower right: Longitude vs. VTEC.

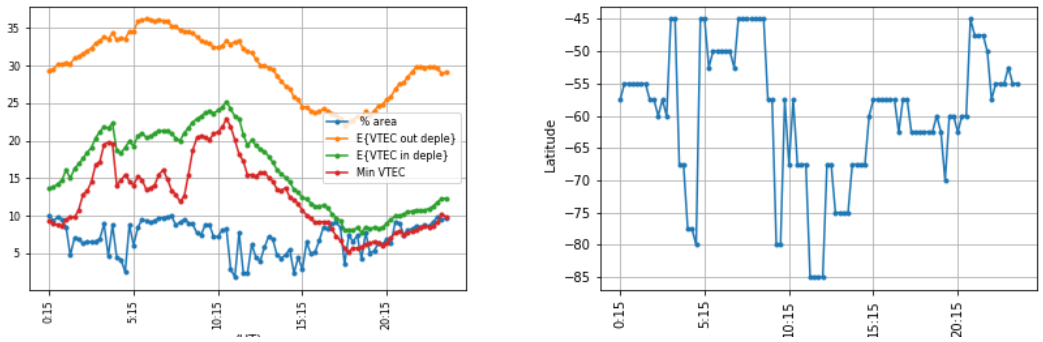

Fig. 9. South 2001/051. **Left**. Blue: % of the area of the detected depletion, Red: minimum the VTEC in the depleted region, Green: mean value of the VTEC in the depleted region, Orange: mean value of the VTEC out of the depleted region. **Right**: the trajectory of the latitude of the minimum VTEC value along time.

23:45 UT) and for comparison purposes, a different moment in the same day (08:30 UT) where no trough was reported. The criterion for choosing the 08:30 UT map has been the distinct behavior of the VTEC distribution at this time compared to the rest of the day, as seen in Figure 17. Around this moment there is a rapid decrease in the detected depletion area, together with a marked decrease in the minimum VTEC value, while the VTEC value outside the depletion area remains constant at a value three times higher.

The authors of the paper [voiculescu (2016)] obtained the experimental data come from the European Incoherent Scatter (EISCAT) radars. EISCAT is a scientific association operating incoherent scatter radar systems in northern Scandinavia. The EISCAT aimed to study ionospheric and magnetospheric processes, and the authors used the radars for analyzing some properties of postmidnight troughs in summer in sunlit plasma. Although the measurements are done in the month of May the authors define for their study the summer comprising the interval from May to August. One of the critera for selecting the days in their study was that the Geomagnetic activity was low during all events, with K_p between 0 and 2.

In Figure 14 we see that the minimum of ionization is

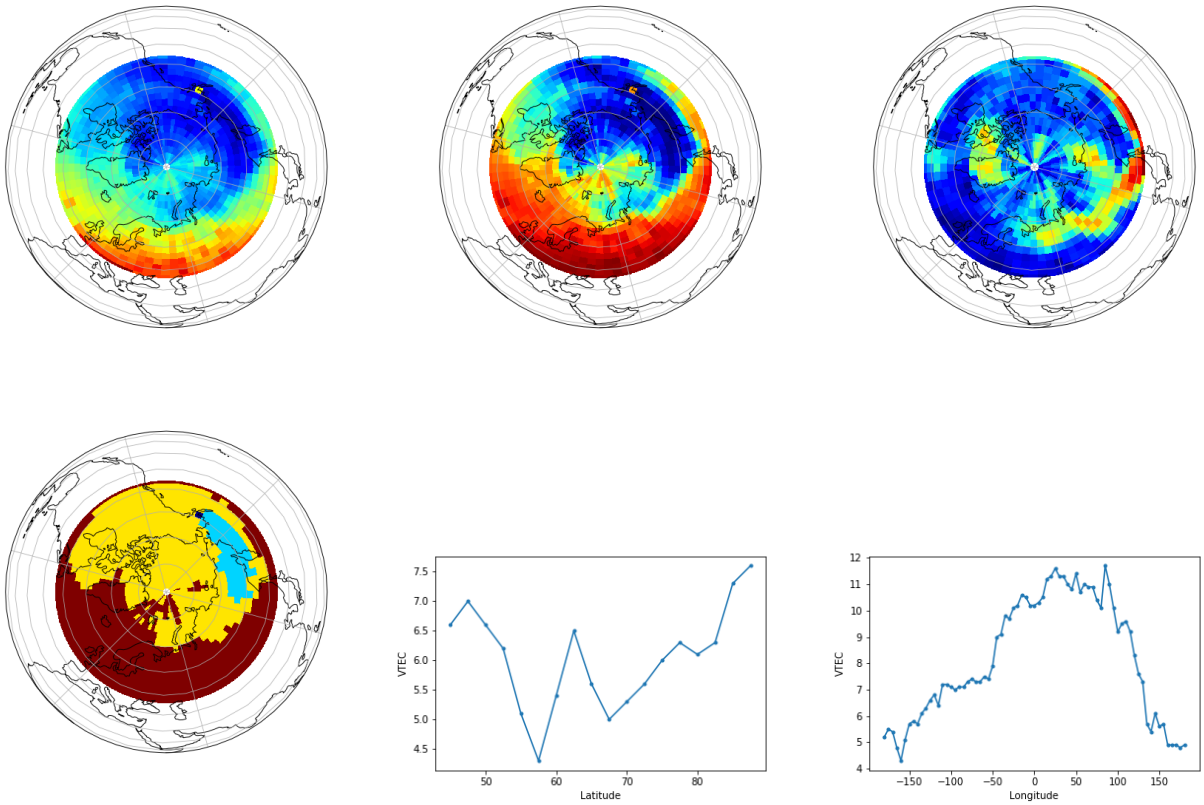

Fig. 10. North Pole GNSS Polar Map 2007/210 at 13:45 (UT) (Summer) Upper left: VTEC map. Upper middle: equalized map. Upper right, spatial gradient of the equalized map. Lower left: detected depletion in light blue. Lower middle: VTEC vs. latitude. Lower right: VTEC vs. Longitude.

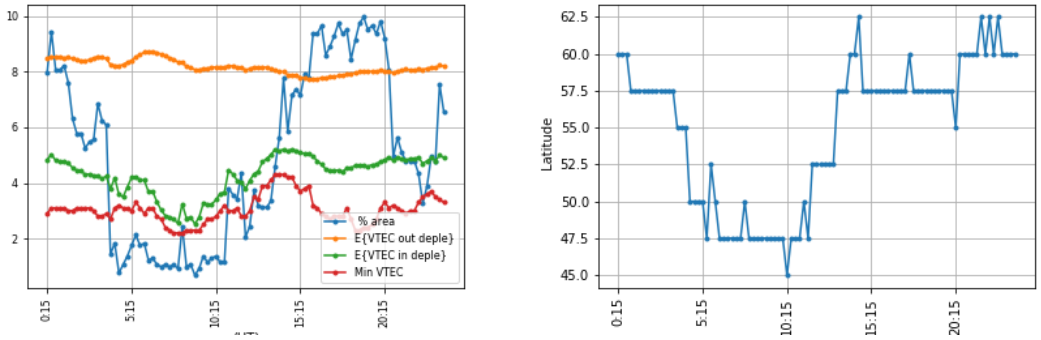

Fig. 11. North 2007/210 . **Left**: Blue: % of the area of the detected depletion. Red: minimum the VTEC in the depleted region. Green): mean value of the VTEC in the depleted region. Orange: mean value of the VTEC out of the depleted region. **Right**: the trajectory of the latitude of the minimum VTEC value along time.

TABLE III
MAPS ANALYSED IN THIS SECTION.

Year/day	Time	Figure number
2004/138	North Pole 08:30 (UT) Spring	14
2004/138	North Pole 22:30 (UT) Spring	15
2004/138	North Pole 23:45 (UT) Spring	16
2004/138	North Pole VTEC Time evolution	17

located at a latitude of approximately 50° degrees, with a VTEC value approximately 5 times lower than the maximum and 3 times lower than the mean value. The equalized map divides the map into three ionization zones. In the Alaska region, the spatial gradient emphasizes the transition between the high and medium ionization regions and appears as a barrier between regions. On the other hand, unlike the maps presented in other sections of this article, in the minimum area, the gradient indicates a small variation of ionization, i.e., locally flat with a level almost equal to the minimum value. The result is a region of low ionization, where the average ionization is about half (see Latitude/Longitude vs. VTEC in the lower row of Figure 14 and the time evolution in Figure

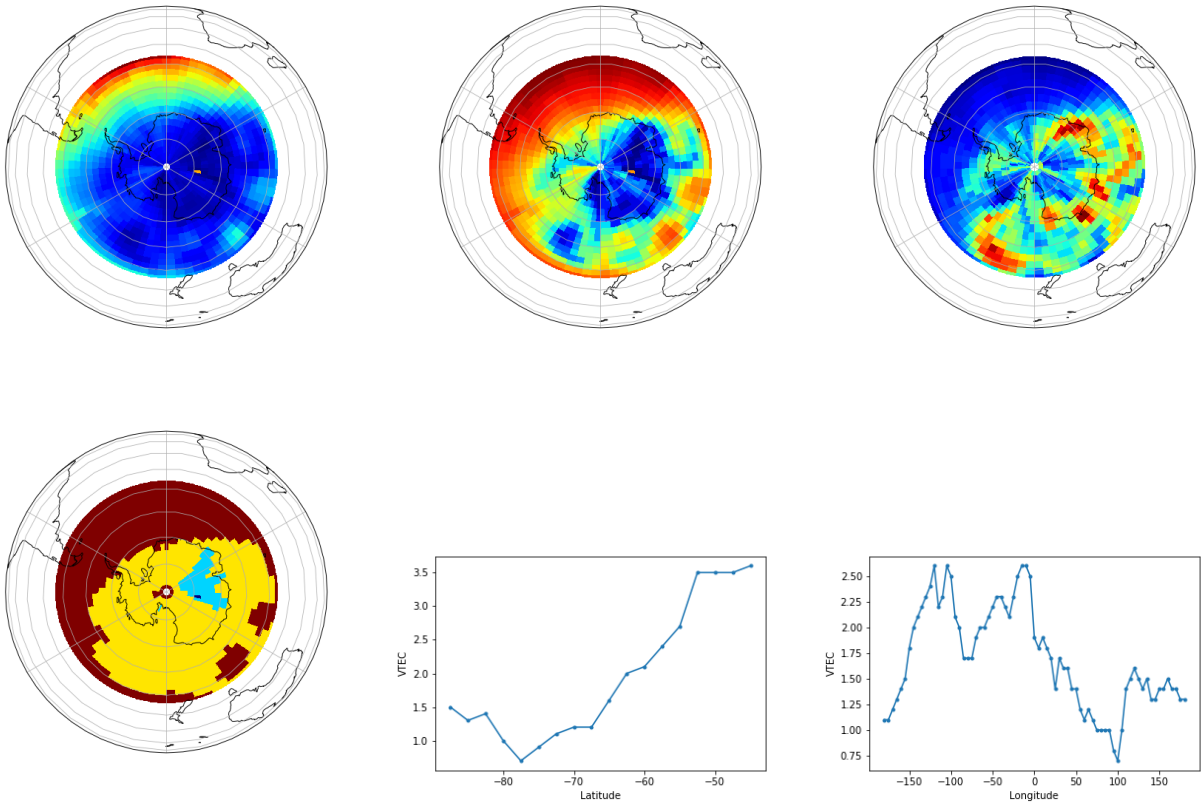

Fig. 12. South Pole GNSS Polar Map 2007/210 at 13:45 (UT) (Winter) Upper left: VTEC map. Upper middle: equalized map. Upper right, spatial gradient of the equalized map. Lower left: detected depletion in light blue. Lower middle: VTEC vs. latitude. Lower right: VTEC vs. Longitude.

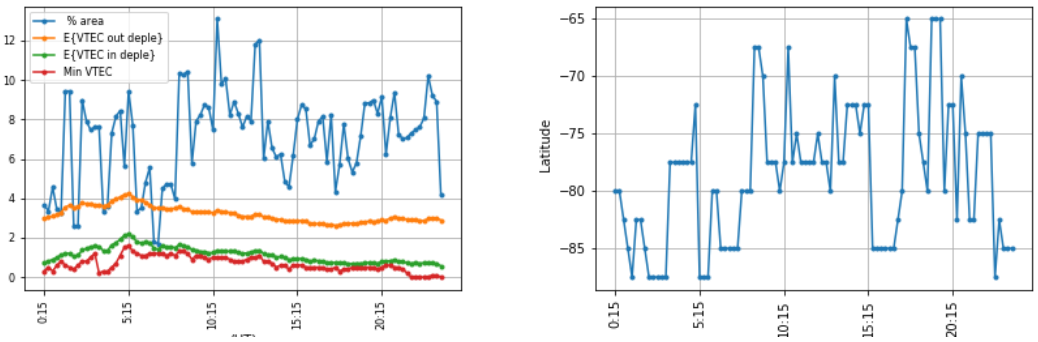

Fig. 13. South 2007/210 . **Left**: Blue: % of the area of the detected depletion. Red: minimum the VTEC in the depleted region. Green: mean value of the VTEC in the depleted region. Orange: mean value of the VTEC out of the depleted region. **Right**: the trajectory of the latitude of the minimum VTEC value along time.

17).

The next example is related to the troughs reported in the paper, which correspond to the case 2004/138 at 22:30 UT in Figure 15 and at 23:45 UT in Figure 16. In the paper, the authors report at this moment a trough at about latitude 75°, which in Figure 15 appears as a clear depletion concerning the surroundings at the same latitude, and to a lesser extent in Figure 16.

The region reported in the article as a trough is also well defined in the equalized map. Furthermore, the algorithm can to detect discontinuous depletions, in this case, it does not detect the trough at latitude 75°. The reason why the algorithm has not reported two depletions (i.e. at latitudes 53° and 75°) is that the VTEC level corresponding to the 75° trough is located in a plateau and is three times higher than the minimum value. Since the algorithm we propose is based on using thresholds related to percentiles, the depletion located at the plateau will not be detected. Note that if instead of taking maps between 45° and 90° we had taken the interval 65° and 90°, these troughs would have been detected. This range between latitudes 65° and 90° degrees, was the one used by [voiculescu (2016)].

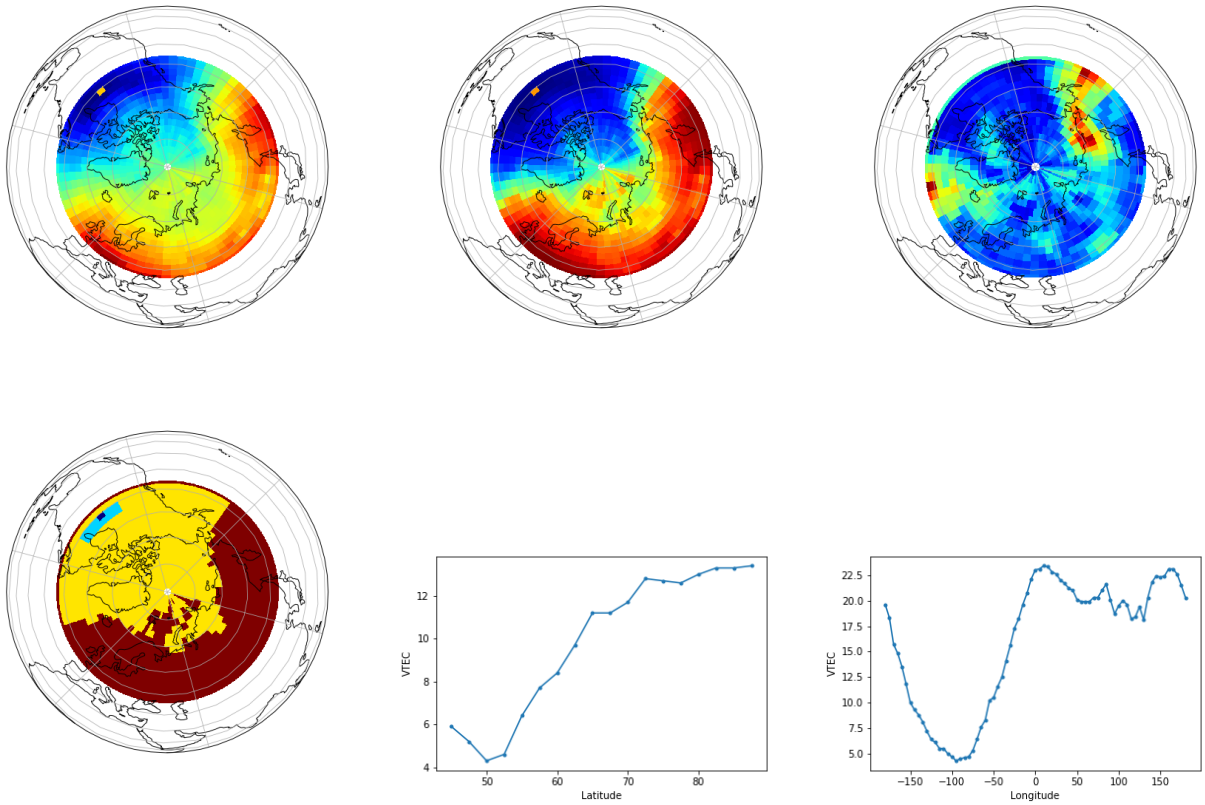

Fig. 14. North Pole GNSS Map 2004/138 at 08:30(UT) Upper left: VTEC map. Upper middle: equalized map. Upper right, spatial gradient of the equalized map. Lower left: detected depletion in light blue. Lower middle: VTEC vs. latitude. Lower right: VTEC vs. Longitude.

The temporal evolution of the parameters (Figure 17) of the identified depletion shows that between 20:00 UT and 00:00 UT the area and minimum and average value of VTEC in the depletion hardly change. However, the features displayed in the figure correspond to the depletion detected at latitudes between $52°$ and $58°$ degrees, which have VTEC levels at least half those associated with the troughs reported in the article.

The case analyzed in this example leads us to consider a potential future improvement of the algorithm based on determining a histogram of the VTEC levels and based on the modes that appear in the histogram, decide the number of levels that are taken to allow the algorithm to generate the flow process that determines regions of relative depletion. This would allow us to detect depletion regions at levels of ionization that might defer significantly.

E. Polar Depletion corresponding to 2007/285 and 2007/068

In the [Zou (2011)], the authors report the presence of storm-related mid-latitude troughs. In this article, we will compare the results they report with our method for Oct. 12, 2007 (2007/285) and Mar. 08, 2008 (2007/068). In addition to detecting the troughs reported in the article, an additional region of depletion was detected. The troughs were detected at the reported coordinates.

We show the results for the storm of Mar. 08, 2008 (2007/068) in Figures 18 and 19. In the article [Zou (2011)],

TABLE IV
MAPS ANALYSED IN THIS SECTION.

Year/day	Time	Figure number
2007/285	North Pole 14:00(UT) Autumn	18
2007/285	North Pole Time evolution VTEC	19
2008/068	North Pole 09:45(UT) Spring	20
2008/068	North Pole Time evolution VTEC	21

the authors indicate that the onset of the storm is at 11:20 UT, which in Figure 19 appeared as a rapid oscillation of the area of depletion and the passage of the location of the minimum VTEC from $68°$ degrees to $53°$ degrees. However, the value of the minimum and average ionization in the depletion zone hardly varies. Figure 18 shows the map around the end of the storm at 14:00 UT. The point of lowest ionization coincides with the position reported in the article, i.e., in the Alaskan region. The equalized map shows a low ionization band with areas of local change that are more clearly observed in the spatial gradient map, indicating the presence of two separated regions. The algorithm detects two low depletion zones, with a second depletion zone located at $100°$ degrees north of Siberia, with a slightly higher ionization level than Alaska. At approximately 15:15 UT there is a rapid drop in the area of the depletion, which matches a drop in the minimum and average VTEC value, while the area surrounding/outside the depletion region maintains a trend of increasing VTEC.

We present the analysis for the storm of Oct. 12, 2007 in

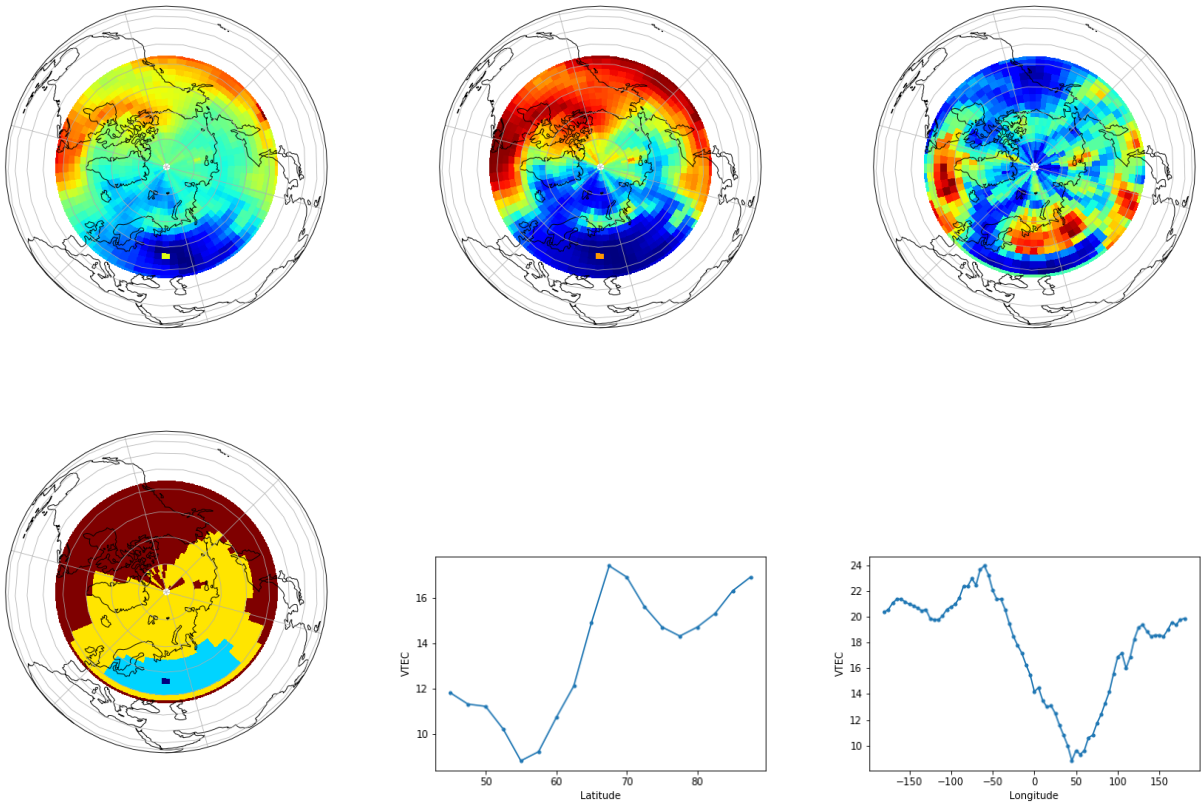

Fig. 15. North Pole GNSS Map 2004/138 at 22:30(UT) Upper left: VTEC map. Upper middle: equalized map. Upper right, spatial gradient of the equalized map. Lower left: detected depletion in light blue. Lower middle: VTEC vs. latitude. Lower right: VTEC vs. Longitude.

Figures 20 and 21. The authors report a storm that occurred at 11:40 UT as measured by ground magnetometer signatures. Figure 21 shows that from 9:00 when the authors of [Zou (2011)] indicate that it is a quiet time, there is an increase in VTEC values, along with a shift of the position of the minimum VTEC from latitude $67°$ degrees to $85°$ degrees. At 10:15 UT, there is a rapid change in latitude from the minimum VTEC, shifting to $53°$ degrees, where it remains for the duration of the storm reported by [Zou (2011)]. At the same time, the area of the depletion region increases. This increase in area tracks the increase of the ionization level. Then descends quickly at the end of the storm which according to the authors occurs at 16:00 UT. This coincides with a minimum VTEC shift from latitude $53°$ to $62°$ degrees, where it remains for the rest of the day, except at 23:00 UT. At 23:00 UT, there is a rapid increase in the depletion area that coincides with a change in the position of the minimum ionization from latitude $63°$ to latitude $70°$ degrees.

IX. Conclusion

In this article, we have introduced a method for estimating ionization depletion regions in polar areas and tested the properties. We have tested the properties and performance of the algorithm under various conditions including troughs, storms, quiet times, different seasons, and different times of the solar cycle. The method for determining the depletion regions is based on image processing techniques. Specifically, a process of equalization of the GIM map is performed taking the VTEC values as if they were gray levels, then the image gradient is calculated and finally, an image segmentation algorithm based on the watershed technique is applied. The method works in real-time, being the processing time of the order of milliseconds. The algorithm can detect the depletions reported in the literature and track the change in the morphology of the depletions. The method has been implemented as real-time service available at [IONSAT (2020)], which we define with the acronym UPC-Ionsat Real-Time Polar Depletion Estimation Service, UI-RT-PDES, which has been working in real-time since the month of May 2020. The service provides the polar GIMs, the equalized polar GIMs to improve the visualization, and also the depleted regions in the GIMs.

Appendix A
Image Equalization process

The equalization process, consists on finding a mapping for assigning certain values of intensity (VTEC values), to another scale, using a transformation that is monotonously increasing and non linear, i.e. the slope is not uniform. The idea is to assume that the histogram of pixel values x of the original image corresponds to a probability density function $f_x(x)$ of a random variable of the pixels, and use the formula for finding the functional transformation $y = g(x)$ of a random variable to obtain a specific form of a new probability density function $f_y(y)$. In the case of histogram ecualization case the target

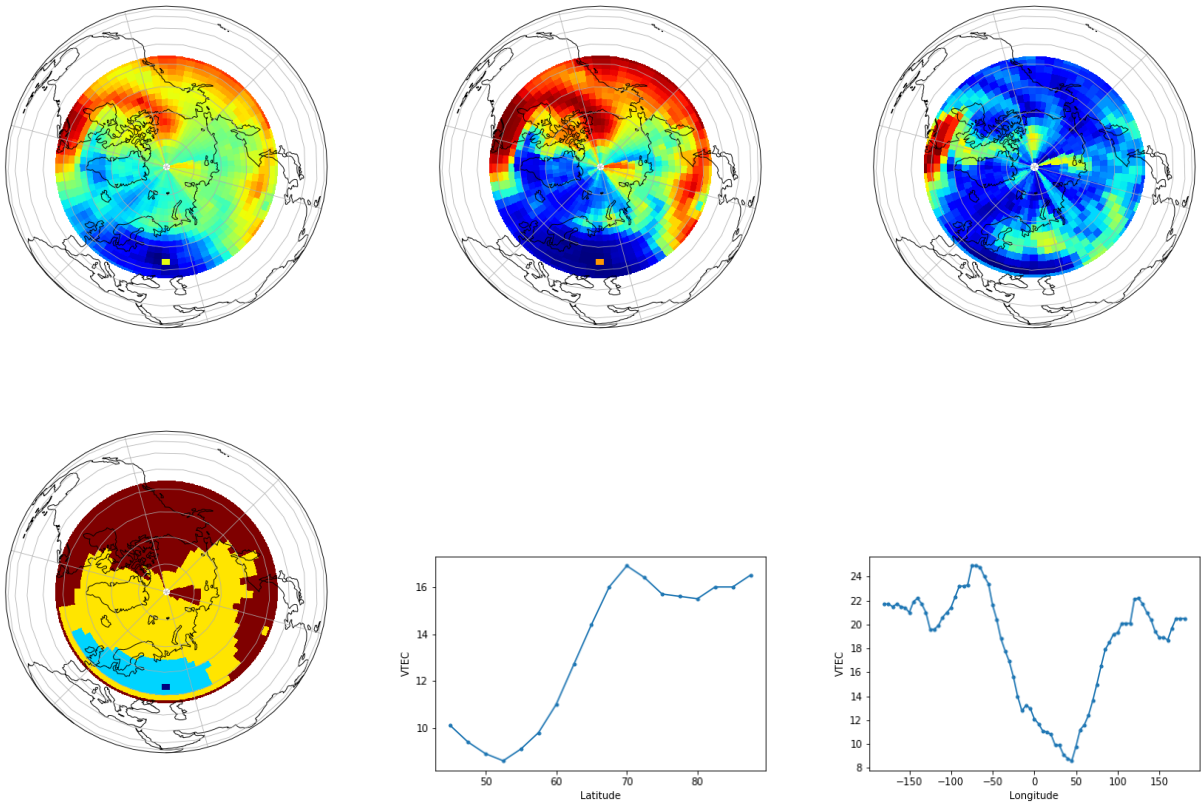

Fig. 16. North Pole GNSS Map 2004/138 at 23:45(UT) Upper left: VTEC map. Upper middle: equalized map. Upper right, spatial gradient of the equalized map. Lower left: detected depletion in light blue. Lower middle: VTEC vs. latitude. Lower right: VTEC vs. Longitude.

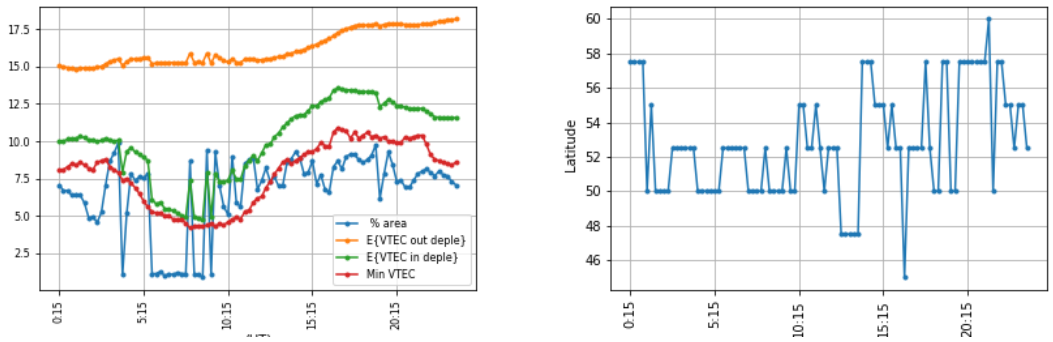

Fig. 17. 2004/138 . Left: (Blue) % of the area of the detected depletion (area: $74.70 \times 10^6 km^2$), (Red) minimum the VTEC in the depleted region, (Green) mean value of the VTEC in the depleted region, (Orange) mean value of the VTEC out of the depleted region. Right: the trajectory of the latitude of the minimum value of VTEC along time.

distribution is the uniform distribution (see [Gonzalez(1984)]). The transformation $g(x)$ is determined by the relation: $f_y(y) = f_x(x)/|g'(x)|$, where $f_y(y) = 1$. The domain of the $f_y(y)$ is $y \in \{0-1\}$. Thus the transformation function function $g(x)$ is computed as $y_0 = g(x_0) = \int_0^{x_o} f_x(x)dx$, which in practice is computed as cumulative sum of the histogram values of the input image. This process is shown in Figure 22, that corresponds to the histogram of the polar GIM shown in Figure 5 (Upper left), note that in the histogram maximum value of VTEC normalized to 1.0. The histogram associated with the map polar GIM has most of the VTEC values ($> 85\%$) in the low range, that is, in the interval $[0-3.5]$. The transformation function $g(x)$ that equalizes the histogram, maps the interval $[0{-}3.5]$ to the interval $[0{-}7.5]$, therefore expanding the margin of values in the blue region of Figure 5 (Upper left) to a margin with higher contrast as can be seen in Figure 5 (Upper middle), where the location of the depleted regions can be seen easily. Note that the transformation as defined will be increasingly monotonous, which preserves the relationship of order. Also, as the integral is approximated by a sum of truncated values, the histogram is not completely flat, but shows oscillations around an average value.

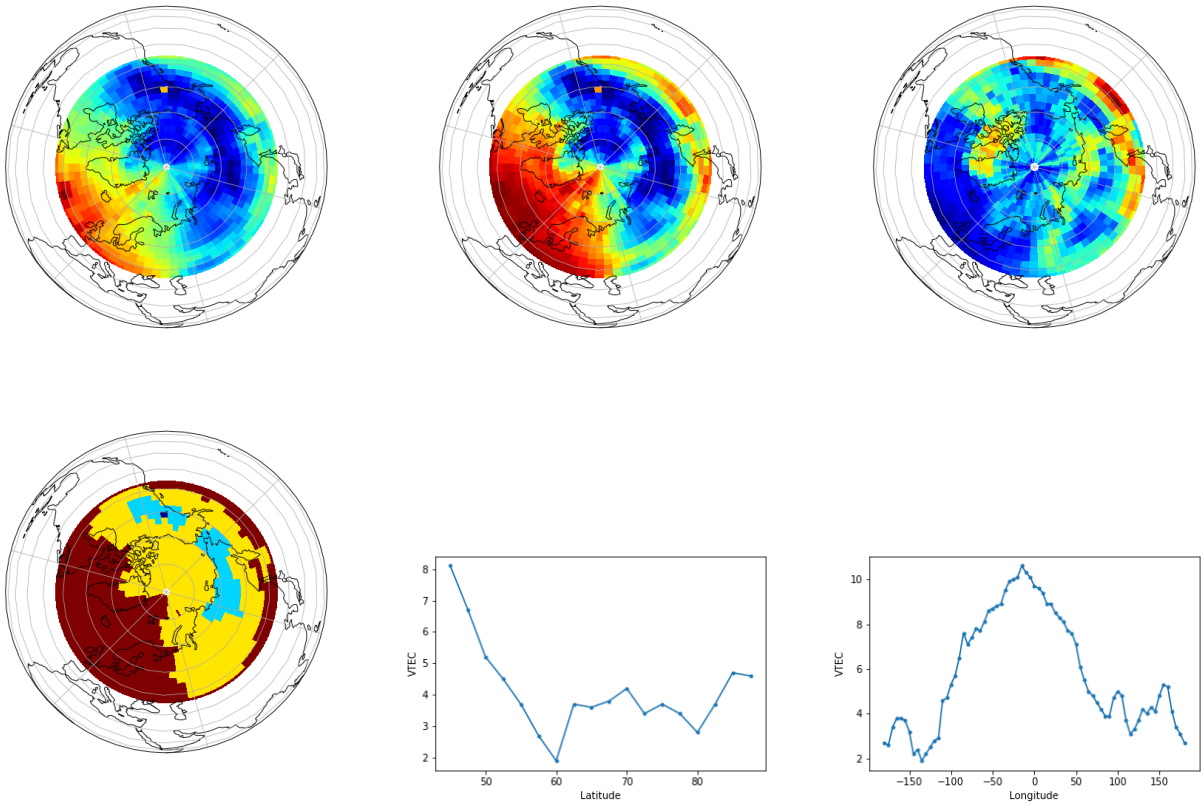

Fig. 18. GNSS Polar Map 2007/285 at 14:00(UT) Upper left: VTEC map. Upper middle: equalized map. Upper right, spatial gradient of the equalized map. Lower left: detected depletion in light blue. Lower middle: VTEC vs. latitude. Lower right: VTEC vs. Longitude.

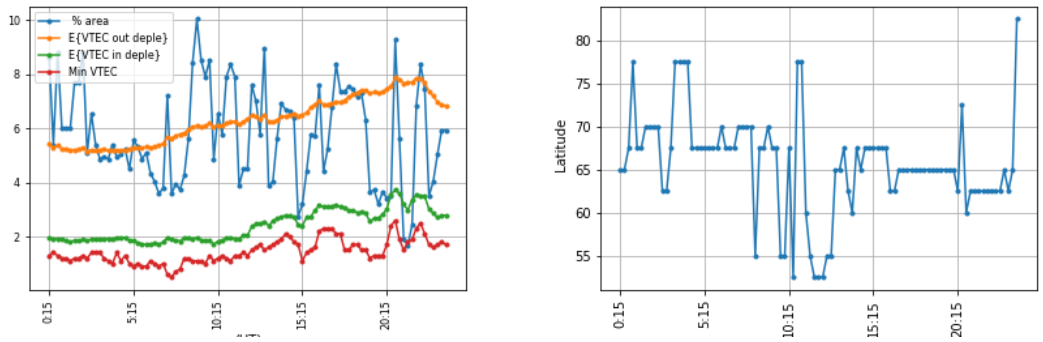

Fig. 19. 2007/285 at 14:00(UT). Left: (Blue) % of the area of the detected depletion (area: $74.70 \times 10^6 km^2$), (Red) minimum the VTEC in the depleted region, (Green) mean value of the VTEC in the depleted region, (Orange) mean value of the VTEC out of the depleted region. Right: the trajectory of the latitude of the minimum value of VTEC along time.

ACKNOWLEDGMENT

This work was supported by the project PID2019-107579RB-I00 (MICINN), and EC- funded activity PolarGIMs2

REFERENCES

[IONSAT (2020)] http://chapman.upc.es/.trial_polar_trough/tomion/real-time/quick/archive/2020/ **2020**.

[EU Arctic Policy 1 (2020)] https://eeas.europa.eu/arctic-policy/eu-arctic-policy_en

[EU Arctic Policy 2(2020)] https://www.arctic-council.org/index.php/en/our-work2/8-news-and-events/489-tfica-dc,

[EU Arctic Policy 2(2020)] https://arkki-project.org/seminar/

[Rodger (1992)] Rodger, AS and Moffett, RJ and Quegan, S, The role of ion drift in the formation of ionisation troughs in the mid-and high-latitude ionosphere—A review. *Journal of Atmospheric and Terrestrial Physics* 54(1), pp.1–30 1992, Elsevier.

[Moffett (1983)] Moffett, RJ and Quegan, S, The role of ion drift in the formation of ionisation troughs in the mid-and high-latitude ionosphere—A review. *Journal of Atmospheric and Terrestrial Physics* 45(5),pp.315–343 1983, Elsevier.

[Van der Walt(2014)] Van der Walt, Stefan and Schönberger, Johannes L and Nunez-Iglesias, Juan and Boulogne, François and Warner, Joshua D and Yager, Neil and Gouillart, Emmanuelle and Yu, Tony, scikit-image: image processing in Python. *PeerJ* 2014, *2*, e453.

[Beucher (1979)] Beucher, S and Lantuejoul, C. Real-Time Edge and Motion

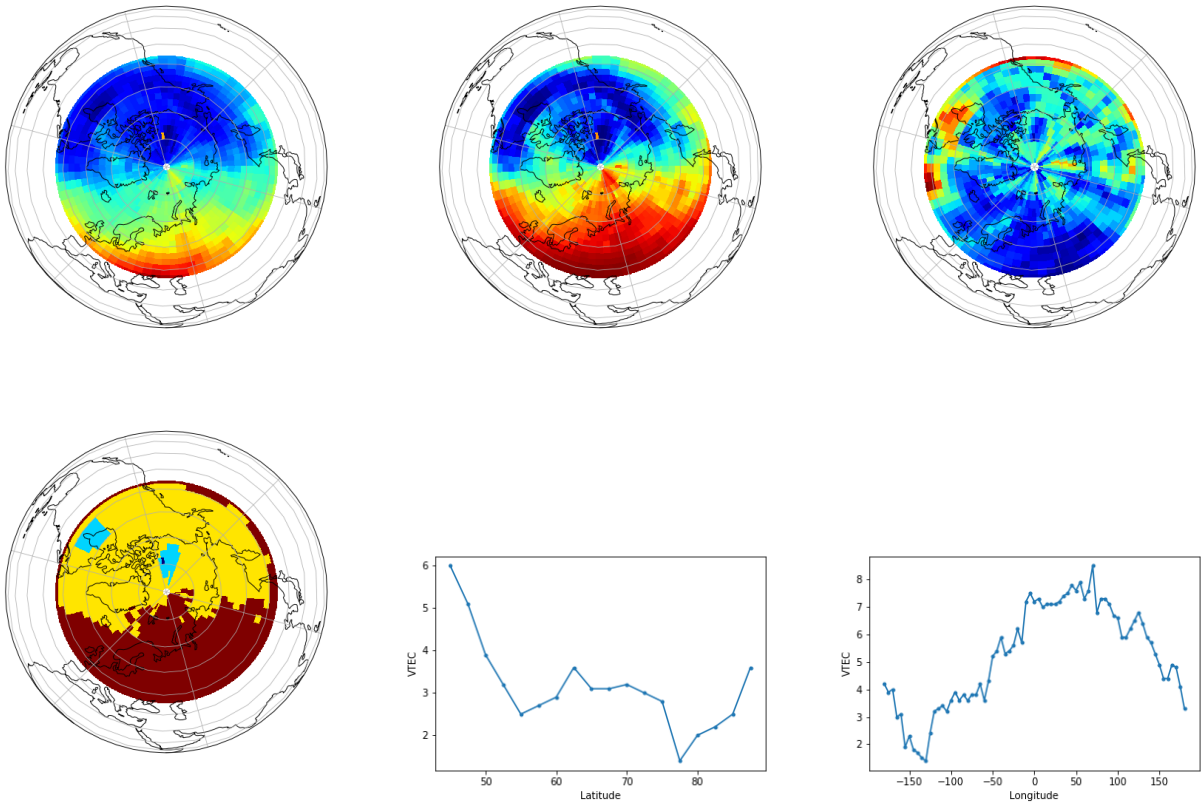

Fig. 20. GNSS Polar Map 2008/068 (09:45(UT)) Upper left: VTEC map. Upper middle: equalized map. Upper right, spatial gradient of the equalized map. Lower left: detected depletion in light blue. Lower middle: VTEC vs. latitude. Lower right: VTEC vs. Longitude.

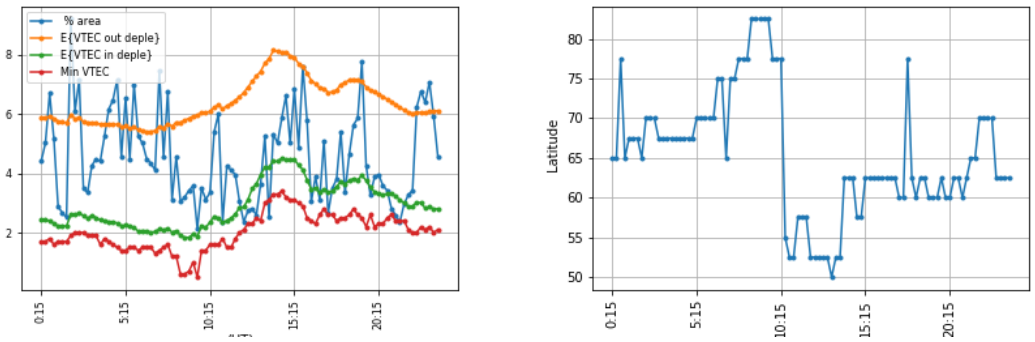

Fig. 21. 2008/068. Left: (Blue) % of area the detected depletion (area: $74.70 \times 10^6 km^2$), (Red) minimum the VTEC in the depleted region, (Green) mean value of the VTEC in the depleted region, (Orange) mean value of the VTEC out of the depleted region. Right: trajectory of the latitude of the minimum value of VTEC along time.

Detection/Estimation. In *1979 International Workshop on Image Processing*.

[Gonzalez(2007)] Gonzalez, Rafael C and Woods, Richard E, Digital Image Processing. *Addison-Wesley Longman Publishing Co., Inc.* 2001.

[Marquez-Neila(2013)] Marquez-Neila, Pablo and Baumela, Luis and Alvarez, Luis, A morphological approach to curvature-based evolution of curves and surfaces. *IEEE Transactions on Pattern Analysis and Machine Intelligence*. 2013, 36(1), pp. 2–17

[Shi (2000)] Shi, Jianbo and Malik, Jitendra, Fernand. Normalized cuts and image segmentation. In *2000 IEEE Transactions on pattern analysis and machine intelligence*; 2000; 22(8) pp. 888–905.

[Gonzalez(1984)] Athanasios Papoulis, Random Variables, and Stochastic Processes. *McGraw-Hill.* 1984.

[Meyer (1992)] Meyer, Fernand. Color image segmentation. In *1992 International Conference on Image Processing and its Applications*; IET; pp. 303–306, 1992.

[Neubert(2014)] Neubert, Peer and Protzel, Peter. Compact watershed and preemptive slic: On improving trade-offs of superpixel segmentation algorithms. In *2014 22nd International Conference on Pattern Recognition*; pp. 996–1001; IEEE, 2014.

[Shinbori(2018)] Shinbori, Atsuki and Otsuka, Yuichi and Tsugawa, Takuya and Nishioka, Michi and Kumamoto, Atsushi and Tsuchiya, Fuminori and Matsuda, Shoya and Kasahara, Yoshiya and Matsuoka, Ayako and Ruohoniemi, J Michael and others, Temporal and spatial variations of storm time midlatitude ionospheric trough based on global GNSS-TEC and Arase satellite observations. *Geophysical Research Letters.*; 45(15), pp.7362–7370, 2018.

[karpachev (2019)] Karpachev, AT and Klimenko, MV and Klimenko, VV.

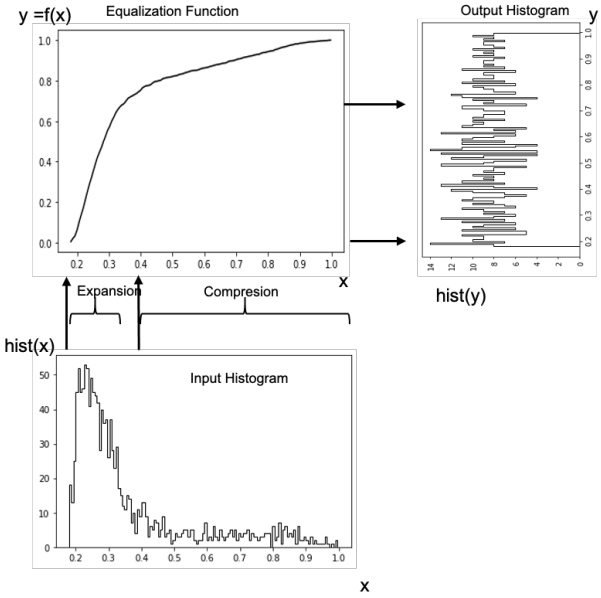

Fig. 22. Diagram of the Histogram Equalization process.

Longitudinal variations of the ionospheric trough position. In *1992 Advances in Space Research*; 63(2),pp.950–966, 2019.

[voiculescu (2016)] Voiculescu, M and Nygrén, T and Aikio, AT and Vanhamäki, H and Pierrard, V. Postmidnight ionospheric troughs in summer at high latitudes. In *Journal of Geophysical Research: Space Physics*; 121(12),pp. 12–171, 2016.

[Zou (2011)] Zou, Shasha and Moldwin, Mark B and Coster, Anthea and Lyons, Larry R and Nicolls, Mike J. GPS TEC observations of dynamics of the mid-latitude trough during substorms. In *Geophysical research letters*; 38(14), 2011.

[Karpachev (2020)] Karpachev, AT and Zhbankov, GA. Additional Horizontal Traces of Ground Reflections on Ionograms from the Interkosmos-19 Satellite in the Night Trough. In *GEOMAGNETISM AND AERONOMY*; 60(1),pp. 58–62, 2020.

[Karpachev (2018)] Norman, R and Carter, Brett A and Healy, SB and Culverwell, ID and Von Engeln, A and Le Marshall, John and Younger, JP and Cate, A and Zhang, Kefei. Ionospheric Regions Producing Anomalous GNSS Radio Occultation Results. In *IEEE Transactions on Geoscience and Remote Sensing*;56(12),pp. 7350–7358 **2018**.

[Hernandez (2020)] Hernández-Pajares, Manuel and Lyu, Haixia and Aragón-Àngel, Àngela and Monte-Moreno, Enric and Liu, Jingbin and An, Jiachun and Jiang, Hu. Polar Electron Content From GPS Data-Based Global Ionospheric Maps: Assessment, Case Studies, and Climatology. In *Journal of Geophysical Research: Space Physics*;125(6),**2020**.

[*Caissy, M., et al.* (2012)] Caissy, M., Agrotis, L., Weber, G., Hernandez-Pajares, M., and Hugentobler, U. The international GNSS real-time service, *GPS world*, 6(23), pp. 52-58, 2009.

[*Li, Z., et al.* (2020)] Li, Z., Wang, N., Hernández-Pajares, M., Yuan, Y., Krankowski, A., Liu, A., and Laurichesse, D. IGS real-time service for global ionospheric total electron content modeling, *Journal of Geodesy*, 94(3),pp. 1-16, 2020.

[*Chernouss,S. A., et al.* (2011)] Chernouss,S. A. and Kalitenkov,N. V. The dependence of GPSpositioning deviation on auroral activity, *International Journal of Remote Sensing*, 32(11),pp.3005-3017, 2011.

[*Dow, J. M., et al.* (2009)] Dow, J. M., Neilan, R., and Rizos, C.: The international GNSS service in a changing landscape of global navigation satellite systems, *Journal of Geodesy*, 83, pp.191–198, 2009.

[*Hernández-Pajares, et al.* (1999)] Hernández-Pajares, M., Juan, J. M., and Sanz, J. New approaches in global ionospheric determination using ground GPS data. *Journal of Atmospheric and Solar-Terrestrial Physics*; 61(16),pp. 1237-1247, 1999.

[*Orús, R., et al.* (2005)] Orús, R., Hernández-Pajares, M., Juan, J. M., and Sanz, J. Improvement of global ionospheric VTEC maps by using kriging interpolation technique. *Journal of Atmospheric and Solar-Terrestrial Physics*; 67(16), pp. 1598-1609,2005.

[*Zishen, et al.* (2013)] Li, Zishen and Yuan, Yunbin and Fan, Lei and Huo, Xingliang and Hsu, Houtse. Determination of the differential code bias for current BDS satellites. *IEEE transactions on geoscience and remote sensing*; 52(7), pp. 3968–3979,2013.

[*Wang, et al.* (2016)] Wang, Ningbo and Yuan, Yunbin and Li, Zishen and Montenbruck, Oliver and Tan, Bingfeng. Determination of differential code biases with multi-GNSS observations. *Journal of Geodesy*; 90(3), pp. 209–228,2016.

[*Orús, R., et al.* (2002)] Orús, R., Hernández-Pajares, M., Juan, J. M., Sanz, J., and García-Fernández, M. Performance of different TEC models to provide GPS ionospheric corrections. *Journal of Atmospheric and Solar-Terrestrial Physics*, 64(18),pp. 2055-2062,2002

[*Hernández Pajares, et al.* (2000)] Hernández Pajares, M., Juan, J. M., Sanz, J., and Colombo, O. L. Application of ionospheric tomography to real time GPS carrier phase ambiguities resolution, at scales of 400 - 1000 km and with high geomagnetic activity. *Geophysical Research Letters*, 27(13), 2009-2012.

[*Feltens, et al.*(2011)] Feltens, J., M. Angling, N. Jackson-Booth, N. Jakowski, M. Hoque, M. Hernández Pajares, A. Aragón Angel, R. Orús, and R. Zandbergen. Comparative testing of four ionospheric models driven with GPS measurements. *Radio Science* 46(6), 2011.

[*Hernández Pajarez, et al.* (2016)] Hernández-Pajarez, Manuel, David Roma Dollase, Andrzej Krankowski, Alberto García Rigo, and Raul Orús Pérez Comparing performances of seven different global VTEC ionospheric models in the IGS context. *International GNSS Service Workshop (IGS 2016): Sydney, Australia* february 8-12, 2016, pp. 1-13. International GNSS Service (IGS), 2016.

[*Roma-Dollase, et al.* (2017)] Roma-Dollase, David, Manuel Hernández-Pajares, Andrzej Krankowski, Kacper Kotulak, Reza Ghoddousi-Fard, Yunbin Yuan, Zishen Li et al. Consistency of seven different GNSS globl ionospheric mpping techniques during one solr cycle. *Journal of Geodesy* pp. 1-16, 2017.

Enrique Monte Moreno Enrique Monte Moreno received the degree on Telecomunication engineering in 1987 by the Universitat Politecnica de Catalunya, the Ph.D. degree in digital signal processing in 1992, a Degree in philosophy in 2000, and a Degree in mathematics in 2010. He is currently an Associate Professor at the Department of Signal Theory and Communications, Universitat Politcnica de Catalunya, Barcelona, Spain. His research interests include digital signal processing, automatic speech recognition, GNSS , machine learning applied to economics, medical topics and the study of the ionosphere.

Manuel Hernandez-Pajares Manuel Hernández-Pajares is Full Professor and Head of research group UPC-IonSAT at "Universitat Politècnica de Catalunya", Barcelona, Spain. He has been working on Global Navigation Satellite Systems (GNSS) since 1989, in new algorithms for precise ionospheric sounding and navigation since 1994. He has been the chair of the International GNSS Service (IGS) Ionosphere WG (2002-2007), and PI of tens of international scientific projects. He has published more than 100 papers in peer reviewed journals within the first and second quartile of impact factor, with more than 5300 citations (h=35 and i10=93). Manuel is also co-authoring 6 patents, most of them international.

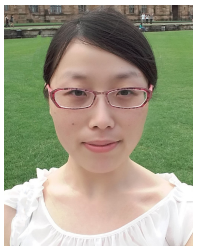

Haixia Lyu Haixia Lyu received her Bachelor degree in 2010, and Master degree in 2012, both from Wuhan University, and she is a Ph.D. candidate at GNSS Research Center, Wuhan University from 2014 and has studied in UPC-IonSAT group from 2016 and worked in IEEC from 2017, where the focus of her current research lies in ionospheric determination using GNSS data.

Heng Yang Heng Yang received his PhD degree in signal theory and processing in 2019 by Universitat Politecnica de Catalunya. He is currently a postdoctoral researcher in the group of IonSAT, at the department of mathematics of Universitat Politecnica de Catalunya, Barcelona, Spain. He is working on the technologies of GNSS ionospheric sounding, including the computation of real-time global ionospheric maps, the detection of ionospheric perturbations and relationship with natural events.

Angela Aragon-Angel Angela Aragon-Angel received his PhD degree in the Department of Applied Mathematics by Universitat Politecnica de Catalunya, and currently works at the Joint Research Centre (JRC), European Commission. Angela does research and consulting in Aerospace Engineering, Plasma Physics and Geophysics. Their current project is Ionospheric modeling.